Composites Part B 292 (2025) 112071

Contents lists available at ScienceDirect

Composites Part B

journal homepage: www.elsevier.com/locate/compositesb

Composite scaffolds based on egg membrane and eggshell-derived inorganic particles promote soft and hard tissue repair

Zhengchao Yuan [a,1], Siyuan Wu [b,1], Liwen Fu [c,1], Muhammad Shafiq [d], Yuqing Liang [b], Peng Li [b], Xinyi Wang [a], Hao Feng [a], Rashida Hashim [e], Shuqi Lou [a], Mohamed EL-Newehy [f], Meera Moydeen Abdulhameed [f], Weifen Zhang [g,**], Xiumei Mo [a,*], Shichao Jiang [b,***]

[a] State Key Laboratory for Modification of Chemical Fibers and Polymer Materials, Shanghai Engineering Research Center of Nano-Biomaterials and Regenerative Medicine, College of Biological Science and Medical Engineering, Donghua University, 201620, Shanghai, China
[b] Department of Orthopedics, Shandong Provincial Hospital Affiliated to Shandong First Medical University, Jinan, 250021, China
[c] Department of Orthopedic Oncology, Shanghai Bone Tumor Institute, Shanghai General Hospital, Shanghai Jiao Tong University School of Medicine, Shanghai, 200080, China
[d] Innovation Center of NanoMedicine (iCONM), Kawasaki Institute of Industrial Promotion, Kawasaki-ku, Kawasaki, 210-0821, Japan
[e] Department of Chemistry, COMSATS University Islamabad (CUI), Lahore Campus, Lahore, 54,000, Pakistan
[f] Department of Chemistry, College of Science, King Saud University, P.O. Box 2455, Riyadh 11451, Saudi Arabia
[g] School of Pharmacy, Shandong Second Medical University, Weifang, 261053, China

ARTICLE INFO

Handling Editor: Dr Hao Wang

Keywords:
Eggshell
Eggshell membrane
Network pharmacology
Inorganic particles
Wound healing
Bone regeneration

ABSTRACT

It is essential to exploit the eggshell membrane (EM) and eggshell (ES) for biomaterial science as a bioresource technology albeit that they are generally considered as waste products of the egg industry. The EM with Janus structural and compositional properties can be prepared into tissue-engineered constructs. The ES was prepared into the inorganic nanoparticles (NPs) namely PCa with an average diameter of 0.67 μm, which was comprised of various inorganic oxides, such as calcium oxide (CaO), and zinc oxide (ZnO). By harnessing the individual advantages of the EM and PCa, they were fabricated into composite scaffolds by a negative pressure inlay method. The composite scaffolds manifested a fibrous network-like structure manifesting large surface area, good mechanical strength (failure force of EM, ca. 1.68 N), biocompatibility and biodegradability *in vitro* and *in vivo*. The EM@Ca3 group enabled efficient hemostasis in the liver trauma injury model (hemostasis time, <32 s), rapid wound healing (96 % at day 14), and bone density similar to the normal bone at week 6 post-implantation. Taken together, our approach of leveraging egg-derived bioresource may be worthy for the future investigations of tissue-engineered constructs and potentially other bio-related disciplines.

1. Introduction

Synthetic polymer-based fibrous scaffolds are widely used for regenerative medicine and tissue engineering (TE) applications, thanks to their controllable biodegradability, high surface area-to-volume ratio, porosity, and tailorable mechanical properties [1]. Physico-chemical properties of synthetic polymer-based scaffolds can be further tailored to afford predictable properties and controllable synthesis [2]. Nonetheless, synthetic polymers, such as polycaprolactone (PCL), polylactide (PLA), and poly(lactic-co-glycolic acid) (PLGA) lack cell recognition motifs and biological activity [3,4]. Alternatively, natural polymers are extensively used as tissue-engineered scaffolds owing to their biocompatibility, biodegradability, and their ability to increase cell-cell and cell-extracellular matrix (ECM) interactions [5,6]. Natural polymers, such as chitosan, cellulose, and sodium alginate possess significant promise in terms of the sustainable and circular economy [7].

The egg shells contain two layers including eggshell membrane (EM), which is flexible in the wet state and eggshell (ES) which is mainly

* Corresponding author.
** Corresponding author.
*** Corresponding author.
E-mail addresses: zhangwf@sdsmu.edu.cn (W. Zhang), xmm@dhu.edu.cn (X. Mo), mailjsc@163.com (S. Jiang).
[1] Z.Y., S.W., and L.F. contributed equally to this work.

https://doi.org/10.1016/j.compositesb.2024.112071
Received 31 July 2024; Received in revised form 1 December 2024; Accepted 4 December 2024
Available online 11 December 2024

comprised of the mineral component. The EM with natural ECM is obtained from the egg, which possesses remarkable mechanical characteristics and biological functions. The EM is regarded as a functional scaffold to fabricate scaffold materials owing to its biocompatibility, biodegradability, stability, and low immunogenicity [6,8]. The EM possess an outer membrane (OM) adjacent to the ES, an inner membrane (IM), and a limiting membrane (LM) near egg white in structure [8]. The mechanical properties of the EM are comparable to the collagenous systems, thanks to its protein mesh-mimetic structure [9]. Given to the low cost and an easy availability of the waste byproduct of the egg from the household industry, it may possess enormous potential to be used as a bioresource technology to afford tissue-engineered scaffolds for soft and hard tissue regeneration alongside fulfilling the principles of a circular economy [9,11].

The EM also possesses different types of bioactive components, including collagen, hyaluronic acid (HA), and dermatan sulfate (DS) alongside several other biomolecules (e.g., proteins, glycosaminoglycans (GAGs), monosaccharides, lipids, etc.) [8]. The EM further exhibits transparent characteristics with more than 80 % transmittance and can be employed as an ideal wound dressing for skin repair and corneal wound healing [8,11]. Consequently, given to the unique structural and compositional properties of the EM, it has been regarded as a material of great interest for TE applications [10,12]. The EM has been used as a traditional wound dressing for the burn wounds in China [8]. The EM may be further tailored to improve its hydrophilicity, anti-oxidative ability, vasculogenic ability, and anti-inflammatory potential, which may also be beneficial to promote tissue repair [13]. Therefore, the EM could be used as a carrier for the incorporation of bioactive components.

The ES from the food industries and consumption is also abundant in the renewable resource of the calcium carbonate ($CaCO_3$) [14]. The ES is

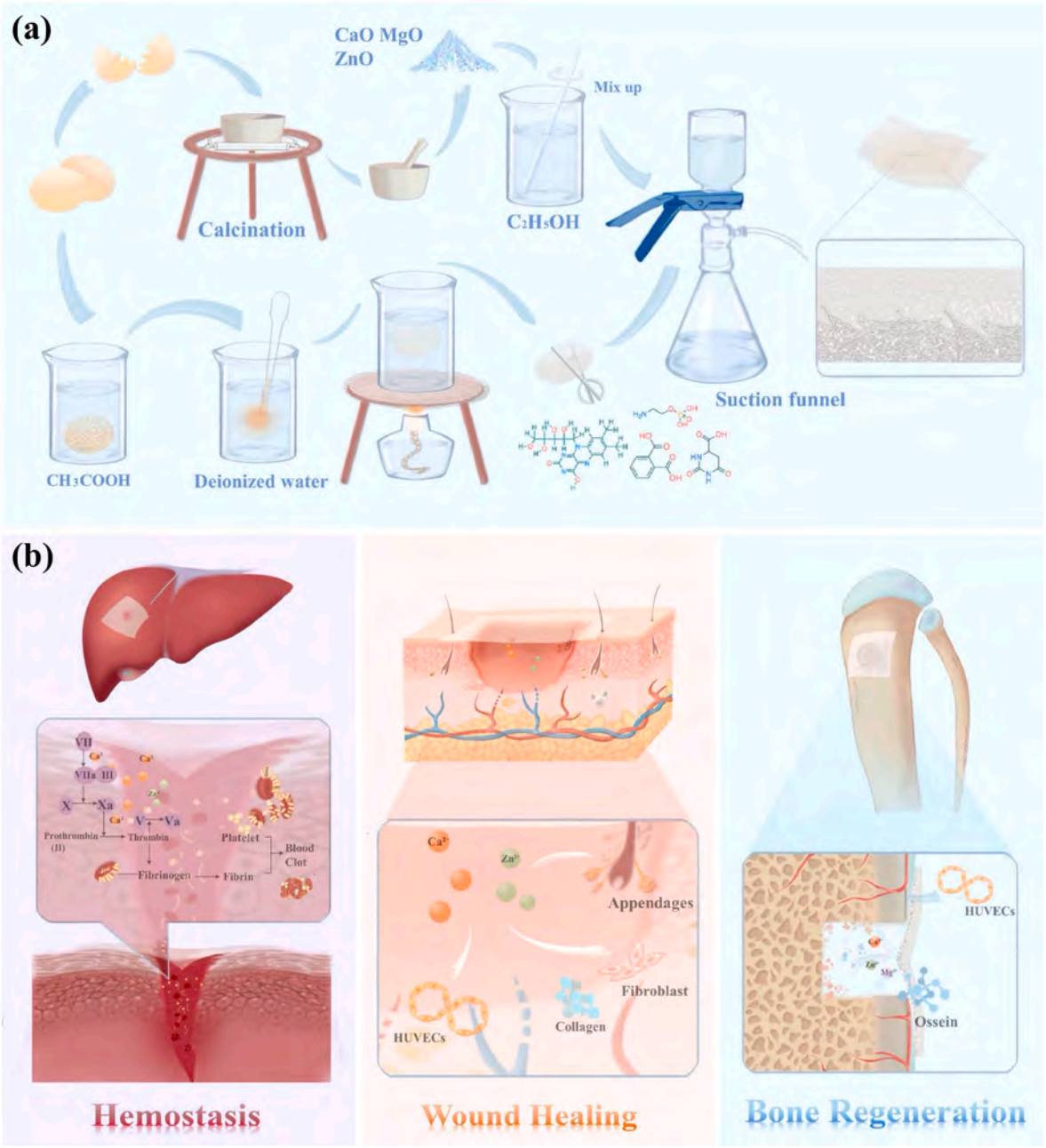

Fig. 1. Overview of the experimental design. (a) Fabrication of the scaffold with EM and PCa particles. (b) Illustration of the dynamic and interactive process mechanism of scaffolds during hemostasis, wound healing, and bone regeneration.

mainly composed of $CaCO_3$ mineral (weight percentage, 96.35 %) alongside smaller amounts of the other minerals, including magnesium carbonate ($MgCO_3$), sodium carbonate (Na_2CO_3), zinc carbonate ($ZnCO_3$), and phosphate [14,15]. The ES could be calcined at 1000 °C for up to 3 h to prepare inorganic nanoparticles namely (PCa) containing calcium oxide (CaO), phosphorous pentaoxide (P_2O_5), zinc oxide (ZnO), magnesium oxide (MgO), and so on [16]. The PCa particles may leverage different types of biological functions, such as angiogenesis, collagen deposition, bone matrix production, and hemostasis [17]. Thus, the PCa could be used as an alternative biomaterial candidate for different types of biomedical application.

The objective of this study was to decipher the structural and compositional properties of the non-heat-treated EM (UEM) and heat-treated EM using untargeted metabolomics analysis. We further carried out network pharmacological analysis of the top 20 untargeted metabolomics component of the EM. The EM and PCa were co-leveraged to synergistically exploit their unique physico-chemical and biological properties to afford composite scaffolds (e.g., EM@Ca1, EM@Ca2, EM@Ca3, etc.) using a negative pressure inlay method (Fig. 1a). We hypothesized that these composite scaffolds may display good hydrophilicity and biocompatibility to potentially promote cell adhesion, cell proliferation, and cell differentiation (Fig. 1b). The biocompatibility of composite scaffolds was discerned using different bio- assays *in vitro* including cytocompatibility and biofunction as well as subcutaneous implantation. These scaffolds were further evaluated for the healing of full-thickness excisional defects and bone defects in rats (Fig. 1b).

2. Experimental

2.1. Materials

The eggs were obtained from the Shanghai Longma market (Shanghai, China). Acetic acid was purchased from Sinopharm Chemical Reagent Co., Ltd (Shanghai, China). The NIH-3T3 fibroblasts and human umbilical vein endothelial cells (HUVECs) were purchased from the Typical Culture Collection Committee Cell Bank (Shanghai, China). The P-control dressing (Nanoderm; National Arms Approval # 20172640268) were purchased from Shandong Namet Biotechnology Co., Ltd (Jinan, China). All other chemicals were of analytical grade from commercial sources and were used without any further purification.

2.2. Preparation of scaffolds

To obtain EM, fresh eggs were placed in 5 % acetic acid solution at room temperature (r.t.) for up to 24 h to afford shell-less eggs; acetic acid solution was changed every 6 h. Shell-less eggs were collected and the opening (diameter, 15 mm) at the end of the air chamber was prepared to remove the egg white as well as yolk components to maintain the integrity EM. Inner side of fresh non-heat-treated EM (UEM) was cleaned with deionized (DI) water until the residual egg white was appeared on the surface for its complete removal. To remove unfavorable residual bioactive substances as well as ensure the removal of the pathogens, the UEM was heated into boiling DI water for up to 10 min to generate EM scaffolds and was further tailored into 5 cm × 4 cm size for the subsequent use.

To prepare the PCa, the ES was obtained from the egg shells. Briefly, the fresh egg was broken from the middle and the EM was carefully cleaned to obtain ES. The ES was ground into fine particles and was calcined at 1000 °C in a muffle furnace (Yamato Scientific Co., Ltd, FO711, Shanghai, China) for up to 3 h. Calcined ES particles were further ground to prepare the PCa power. About 100 mg of PCa power was dispersed into 100 mL of absolute ethanol and large particles of PCa were removed using an 1800 mesh screen (Jiufeng Co., Ltd, 1800, Hebei, China) (Interception of particles larger than 10 μm in diameter). The PCa/ethanol dispersion was dried in a fume hood at r. t. to obtain the PCa powder.

To prepare EM scaffolds loaded with different content of PCa, PCa particles were weighed and dispersed in 10 mL of absolute ethanol to prepare the suspension (content of PCa particles: 1 mg, 5 mg, and 10 mg). The LM side of the EM (5 cm × 4 cm) was tightly attached to the surface of the suction funnel, and ethanol suspension containing PCa particles was added from the OM side (Fig. 1a). The composite scaffolds were dried in a fume hood for up to 2 h at r. t. The scaffolds containing 1 mg, 5 mg, and 10 mg of PCa particles were named as EM@Ca1, EM@Ca2, and EM@Ca3 scaffolds (EM@Cax), respectively.

2.3. Untargeted metabolomics analysis and network pharmacology analysis

The UEM and EM were used for the identification of metabolites using untargeted metabolomics analysis by the Hang Zhou KaiTai-Bio CO., LTD (Hang Zhou, China) [18]. Appropriate mass of samples alongside 1 mL of extract solution (methanol: H_2O = 75/25, (v/v)) and steel balls were added into centrifuge tube. Samples were ground using a tissue grinder (frequency, 50 Hz and time, 180 s) and were sonicated for up to 30 min in an ice bath. The solution was centrifuged at 12,000 rotations per minute (rpm) for up to 10 min at 4 °C to obtain the supernatant, which was concentrated and dried. Samples were redissolved in 200 μL of 50 % acetonitrile solution, and transferred into the detection bottle for liquid chromatography-mass spectrometry (LC-MS) analysis. The LC-MS was performed using Vanquish UHPLC System (Thermo Fisher Scientific, USA) and ACQUITY UPLC ® HSS T3 (2.1 × 100 mm, 1.8 μm) (Waters, Milford, MA, USA), respectively.

The molecular structural formula of the top 20 untargeted metabolomics component and key words such as “wound healing” and “bone regeneration” were used in the PubChem to identify the targeted gene according the literature [19]. The intersection of the potential targets were imported into the Venn diagram, Protein–Protein Interaction (PPI) Network Analysis, GO (Gene Ontology) Function and KEGG (Kyoto Encyclopedia of Genes and Genomes) Enrichment Analysis [20]. The GO enrichment analysis included three modules: cell composition (CC), biological process (BP), and molecular function (MF), and the top 10 were selected according to the number of involved targets ($p < 0.05$). Meanwhile, KEGG pathway analysis was selected for the top 30 targets ($p < 0.05$), and screened for the signal pathways with high enrichment.

2.4. Physicochemical characterization

Scaffolds were characterized for morphological analysis, elemental analysis, average diameter, particle size, and mechanical properties *in vitro*. The detailed methods are provided in the Supplementary Information.

2.5. Biocompatibility and biological functions of scaffolds in vitro

Biocompatibility including hemocompatibility and cytocompatibility assays, as well as biological functions of scaffolds including Transwell migration assay, tube formation *in vitro,* ALP and ARS assay, and blood clotting assay *in vitro* were performed. The detailed methods are provided in the Supplementary Information.

2.6. Animal experiments

All *in vivo* experiments were approved by the Shandong Provincial Hospital Affiliated to Shandong First Medical University, Shandong, China (No. 2024024).

2.6.1. Biocompatibility in vivo

For the preliminary evaluation of the biocompatibility, scaffolds (e.g., EM, EM@Ca1, EM@Ca2, EM@Ca3, etc.) were subcutaneously implanted into Sprague–Dawley rats (SD; age, 6 weeks, n = 6). Animals

were anesthetized using intravenous (IV) administration of sodium pentobarbital (45 mg·kg^{-1}). The muscle pocket was created via skin incision (4 mm × 4 mm) and scaffolds were implanted into the subcutaneous space (n = 3 per group). The skin pocket was closed with 5-0 silk suture. At 2, 4, and 6 weeks, animals were sacrificed with an overdose of pentobarbital sodium. Samples along with their adjacent tissues as well as main organs, including heart, liver, lung, spleen, and kidney, were harvested 6 weeks post-implantation and fixed with 4 % paraformaldehyde (PFA), paraffin-embedded, and sectioned into slices. The excised organs were stained by hematoxylin and eosin (H&E), while explanted scaffolds were stained with H&E and Masson's trichrome (MT) staining.

2.6.2. Hemostatic ability of scaffolds in vivo

Hemostatic ability of the scaffolds was evaluated in a rabbit liver trauma model. New Zealand white rabbits (age, 4 weeks and weight, 2 kg, $n = 4$) were anesthetized by using IV administration of sodium pentobarbital (45 mg·kg^{-1}) and then randomly divided into 5 groups, including control (gauze), EM, EM@Ca1, EM@Ca2, and EM@Ca3 (3 cm × 3 cm; $n = 4$ per group, different groups implanted at different sites in the injured liver). The abdominal skin was shaved and sterilized. The liver was exposed and wound (length, 2 mm and depth, 2 mm) was made using a sterile scalpel. The scaffolds were covered on the wound site to observe the infiltration of blood into the scaffolds. For quantitative analysis, the videos were recorded for all of the groups until the bleeding was completely stopped during hemostatic evaluation. Pre-weighed samples were used to absorb the blood and the blood loss was calculated gravimetrically.

2.6.3. Wound healing in vivo

Thirty male SD rats (age, 6 weeks) were randomly divided into five groups: *i)* gauze (Control), *ii)* commercial dressing (P-control), *iii)* EM, *iv)* EM@Ca1, and *v)* EM@Ca3 (diameter 10 mm). All rats were anesthetized using IV administration of sodium pentobarbital (45 mg·kg^{-1}). Full-thickness excisional defects (Φ = 10 mm, 5 defects each on the left and right dorsal side of the animal) were created on the dorsal side of the rats. Scaffolds were implanted on the defect side and the wounds were covered with elastic bandage to maintain the long-term effect of the dressing. The fresh dressings were used every 3 days and wounds were photographed at day 0 as well as at day 4, 7, 10, and 14. The repaired skin along with the surrounding tissues was harvested, fixed, and stained with H&E and Masson's trichrome staining at day 14. The wound area was calculated by Eq. (1):

$$\text{Wound area} = \frac{A_t}{A_0} \times 100\% \quad (1)$$

where A_t and A_0 represent the wounds at day 0 and at specified time intervals, respectively.

2.6.4. Bone regeneration in vivo

Twelve male SD rats (age, 6 weeks) were randomly divided into four groups: *i)* control, *ii)* EM group, *iii)* EM@Ca1 group, and *iv)* EM@Ca3 group ($n = 3$). Animals were anesthetized using IV administration of sodium pentobarbital (45 mg·kg^{-1}) and tibial bone defect model was established by electroporation (5000 rpm, 1 min; Globalebo, Tianjin, China) (diameter of the defect, 3 mm). The untreated bone defects were used as a control group. For the preparation of bone defect, the muscles around the tibia were dissected and defect was created. Scaffolds were used to cover the bone defect site and the muscle was returned to its original position. Finally, the muscle was sutured followed by the skin closure with the suture. The rats were randomly euthanized after six weeks post-operatively; tibia was collected for micro-CT analysis. Thereafter, the samples were decalcified, dehydrated and sectioned into 5 μm slices to carry out hematoxylin and eosin (H&E) staining and Masson's trichrome (MT) staining.

3. Results

3.1. Metabolome sequencing and network pharmacology analysis

To delineate variations among the components between the UEM and EM alongside and elucidate functional prediction based on the identified components, high-resolution untargeted metabolomics was carried out both for the UEM and EM collected from the same egg [21]. We identified a total 41 types of primary metabolites, which exhibited high content of carboxylic acids and their derivatives, fatty acyls, organo-oxygen compounds, organo-nitrogen compounds, and pyridines and their derivatives (Figs. S1a–S1b, Supporting Information). Conversely, EM exhibited less content of the aforementioned components than that of the UEM presumably owing to the heat treatment (Figs. S1a–S1b, Supporting Information).

Further analysis of secondary metabolites manifested 60 types of metabolites, including pyrimidines and their derivatives, amino acids, peptides and their analogues, fatty acids and fatty acid conjugates, tertiary amines, dicarboxylic acids and derivatives, and carbohydrates and carbohydrate conjugates (Figs. S2a–S2b, Supporting Information). As observed for the primary metabolites, the UEM exhibited higher content of secondary metabolite, including pyrimidines and pyrimidine derivatives, tertiary amines, isoflavonoid O-glycosides, phosphate esters, and hydroxycinnamic acids and hydroxycinnamic acid derivatives than that of the EM group. On the other hand, EM manifested higher content of amino acids, peptides, and analogues, fatty acids and conjugates, dicarboxylic acids and their derivatives, carbohydrates and carbohydrate conjugates, and amines in comparison to the UEM group (Figs. S2a–S2b, Supporting Information).

The untargeted metabolomics analysis of UEM and EM did not show significant difference in the category of the various components albeit significant variations in the type of the ingredients (Figs. S3a–S3c and Figs. S4a–S4d). Both UEM and EM exhibited 189 types of specific natural components. While UEM exhibited higher content of the components, such as betaine, 1-aminocyclopropanecarboxylic acid, triethylamine, beta-carotene, ethylmethylacetic acid, and genistin than that of the EM, it displayed less content of the components, including methylmalonic acid, palmitic acid, 3-hydroxybenzyl alcohol glucoside, riboflavin, and picolinic acid (Fig. S3a-S3c and Fig. S4a-S4d, Supporting Information). The chemical structure of the top 25 substances identified from the EM exhibited a large number of unsaturated carbon-carbon double bonds, amino (−NH_2) groups, carboxylic (−COOH) groups and other functional groups, implying good hydrophilicity (Fig. 2a). These findings indicate that the heat treatment of the EM may change the composition content, while preserve component type, which is indicative of the heat-mediated structural and functional changes in the EM.

To further elucidate the biological activity as well as potential mechanism for the EM-mediated wound healing and bone tissue regeneration, we used network pharmacology (Fig. 3). The target genes for the top 20 components of the EM as well as for wound healing were analyzed alongside 985 intersecting targets (Fig. 3a). To acquire the core targets, such as AKT1, matrix metalloproteinases 9 (MMP9), mitogen-activated protein kinase 3 (MAPK3), interleukin-1-beta (IL-1β), interleukin-6 (IL-6), tumor necrosis factor-alpha (TNF-α), hypoxia-inducible factor-1 alpha (HIF-1α), epidermal growth factor receptor (EGFR), tumor suppressor p53 (TP53), transforming growth factor-beta 1 (TGF-β1), and so on, targets were organized based on their degree values (Fig. S4, Supporting Information). The gene ontology (GO) enrichment analysis manifested regulation of the cell viability and inflammation in wound healing process, including positive regulation of gene expression, cell proliferation, inflammatory response, extracellular space, focal adhesion, protein binding, and protein kinase activity and so on (Fig. 3c). The KEGG (Kyoto Encyclopedia of Genes and Genomes) enrichment analysis indicated the regulation of cell proliferation, inflammatory response and angiogenesis during skin repair, including various signal pathways, such as TNF-α, phosphatidylinositol-3-kinase

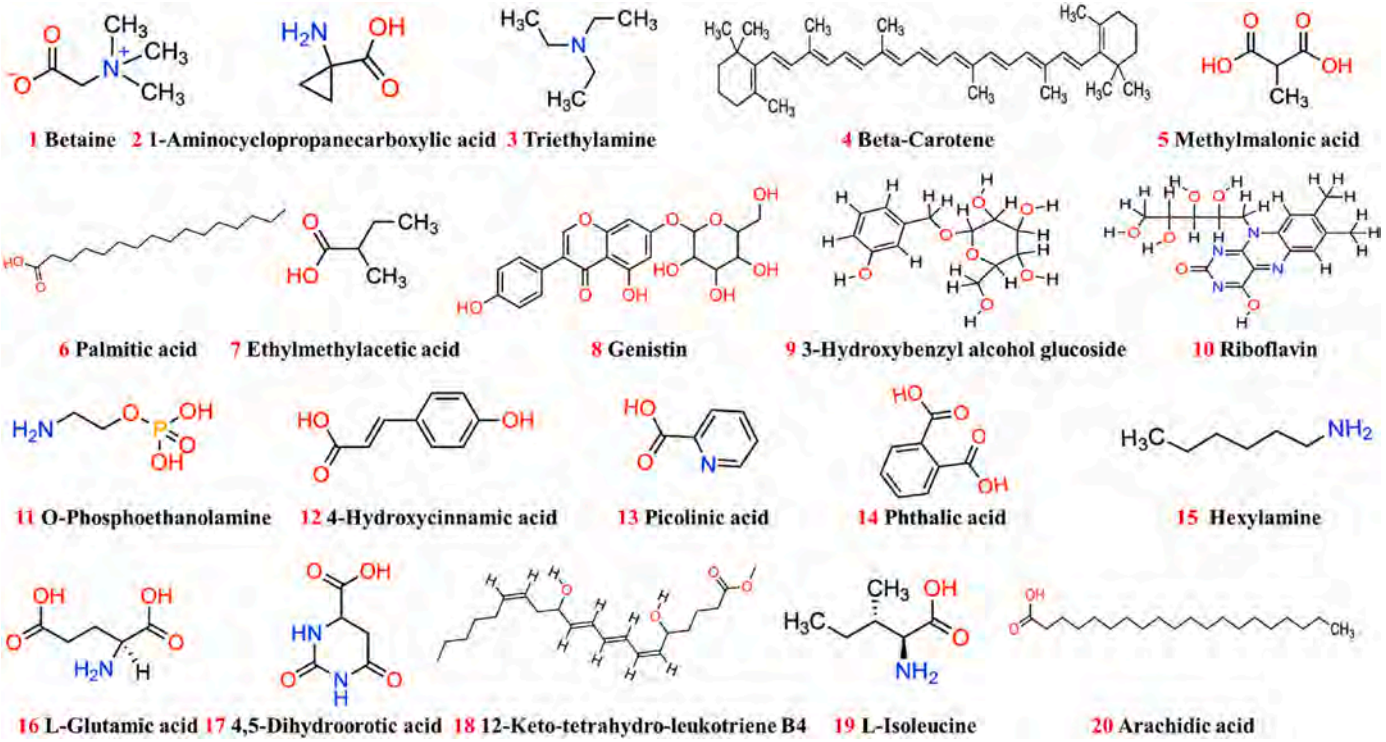

Fig. 2. Chemical structure of the top 20 substances from EM untargeted metabolomics analysis.

(PI3K-Akt), Forkhead box O (FoxO), HIF, and interleukin-17 (IL-17) (Fig. 3d).

We further analyzed the targets of the top 20 untargeted metabolomics components of the EM for bone repair. The intersecting target genes of 899 exert between the top 20 components of EM pointing towards the target genes for bone regeneration, with the core targets, such as MMP9, MAPK3, IL-1B, IL-6, TNF, HIF1A, EGFR, TP53, AKT1, INS, TGF-β1 and so on (Fig. 3b, Figs. S5–S6). The major biological processes involved the positive regulation of the gene expression, inflammatory response, positive regulation of transcription from RNA polymerase II promoter, positive regulation of apoptotic process and so on (Fig. 3e). Cellular components mainly included extracellular space, extracellular region, and focal adhesion and so on (Fig. 3e). On the other hand, the molecular functions mainly included enzyme binding, protein kinase binding, and protease binding (Fig. 3e). The KEGG pathway enrichment analysis also exhibited significant correlation core signaling pathways, including advanced glycation end products-receptor (AGER), PI3K-Akt, TNF, FoxO, HIF-1 and so on (Fig. 3f). These results revealed that the EM had potential anti-inflammatory and tissue remodeling characteristics, which may have implications for bone regeneration. Consequently, we processed EM-based scaffolds and discerned their potential in a full-thickness excisional defect model and a bone defect model.

3.2. Fabrication and evaluation of composite scaffolds

An egg displays a complex ES and membrane structure [22]. Macroscopic shell membrane is composed of flexible EM and $CaCO_3$. The egg shell was removed to afford a milky white egg alongside a hard shell. The ES was calcined to obtain the calcined powder (PCa), which was appeared whitish and granular (Fig. 4a). The PCa was found to be brittle in the dry state and easy-to-break. In contrast, in the wet state, the PCa exhibited good flexibility, which may preserve the integrity of the membrane even after a high degree of curling (Fig. 4b–c, Figs. S9a–b, Supporting Information). The prepared scaffolds did not exhibit sufficient transparency in the dry state, while they exhibited significant light transmittance in the wet state (Fig. 4d, Fig. S9c, Supporting Information). The average size of the PCa particles was 0.67 ± 0.08 μm as revealed by dynamic light scattering (DLS). X-ray photoelectron spectroscopy (XPS) displayed different types of elemental components in the PCa, e.g., calcium (Ca), phosphorous (P), and iron (Fe) (Fig. 4h–i).

Scanning electron microscopy (SEM) showed that the cross-section of the EM was mainly composed of fibers and particles. While the LM was mainly composed of closely-arranged particles, the OM largely exhibited fibers and pores (Fig. 4e). Fibers were gradually decreased while particles were increased during the transition from the OM to the LM. Unlike the OM, which mainly displayed a fibrous structure, the LM was composed of particles with the dense structure alongside a layered, mesh-like, and randomly-oriented fibrous proteinaceous microstructure (Fig. 4e). The thickness of the EM was 43.8 ± 3.66 μm, while the average fiber diameter was 1.97 ± 0.51 μm (Fig. 4j–k). Roughness (Ra) was 46.95 nm and 162.83 nm for LM and OM, respectively, which is indicative of a smooth surface of the LM than that of the OM (Fig. 4f).

To endow the EM with the physiological functions, the PCa and EM were combined to afford multifunctional scaffolds (e.g., EM@Ca1, EM@Ca2, EM@Ca3, etc.). EDS analysis showed the distribution of S and Ca in the EM@Ca1. Moreover, the content of the Ca was gradually increased with an increase in the content of the PCa, thereby indicating that the PCa was successfully loaded into the EM (Fig. 4g & Fig. S10, Supporting Information). The EM manifested brittleness in the dry state, while good flexibility and tensile resistance in the wet state (Fig. S9b, supplementary materials). The EM@Cax scaffolds did not appreciably differ in terms of mechanical properties (Fig. 4m, Figs. S11a–b).

3.3. Hemocompatibility and biocompatibility of scaffolds in vitro

Scaffolds were next examined for hemocompatibility and biocompatibility using NIH-3T3 fibroblasts and HUVECs. Cells were cultured along with the extract solution of various scaffolds. The scaffolds manifested good biocompatibility, both, in the terms of the cell viability and cell cytoskeleton staining for both cell types. It is worthy to note that the scaffolds containing PCa showed significant cell vitality with only a negligible proportion of the apoptotic cells (Fig. 5a–d, Figs. S12a–b).

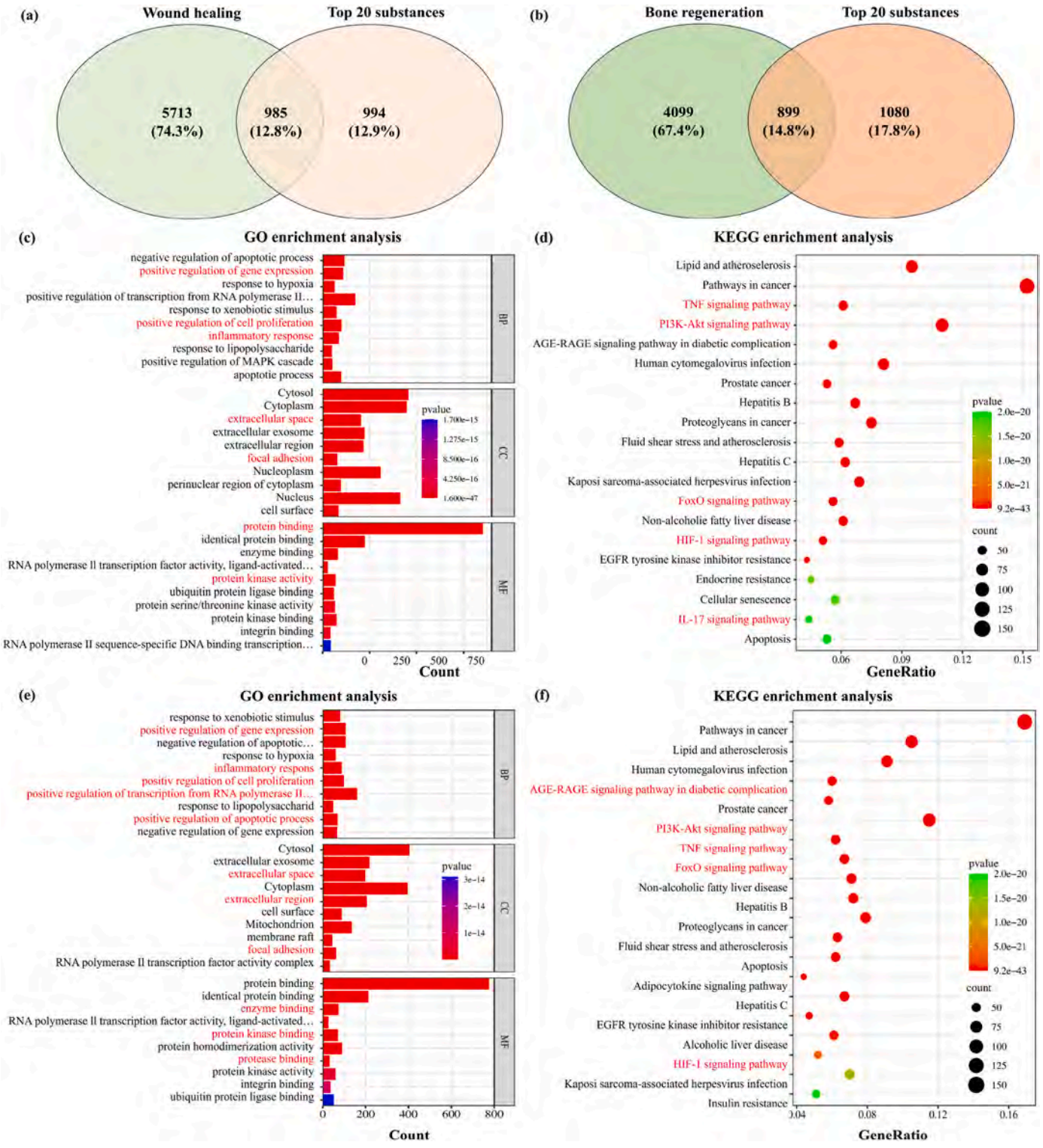

Fig. 3. Network pharmacology analysis. Venn diagram of target intersection between top 20 substances and wound healing (a) as well as top 20 substances and bone repair (b). (c) GO enrichment analysis for the target intersection and (d) target intersection by the KEGG path-way map of top 20 substances and wound healing. (e) Analysis of GO enrichment for target intersection, and (f) target intersection KEGG path-way map of top 20 substances and bone repair.

CCK-8 assay was carried out to discern the proliferation of NIH-3T3 fibroblasts and HUVECs. Both the EM as well as EM alongside PCa manifested a significant tendency to promote cell proliferation in comparison to the control group (Fig. 5e–f). The higher cell viability and proliferation in the EM and EM@Ca scaffolds may be ascribed to the protein components from the EM as well as to the Ca and P elements from the PCa; the latter may also be conducive to the cell proliferation (Fig. 5e–f). All of the scaffolds exhibited negligible hemolysis rate (e.g., 1.03 ± 0.56 %, 0.89 ± 0.25 %, 0.72 ± 0.87 %, and 1.27 ± 0.65 % for EM, EM@Ca1, EM@Ca2, and EM@Ca3, respectively), which was within the acceptable range for the use of the biological materials (<5 %) (Fig. 5g, Fig. S13, Supporting Information) [23]. These data showed sufficient cytocompatibility of the scaffolds, which may also have implications for the *in vivo* studies.

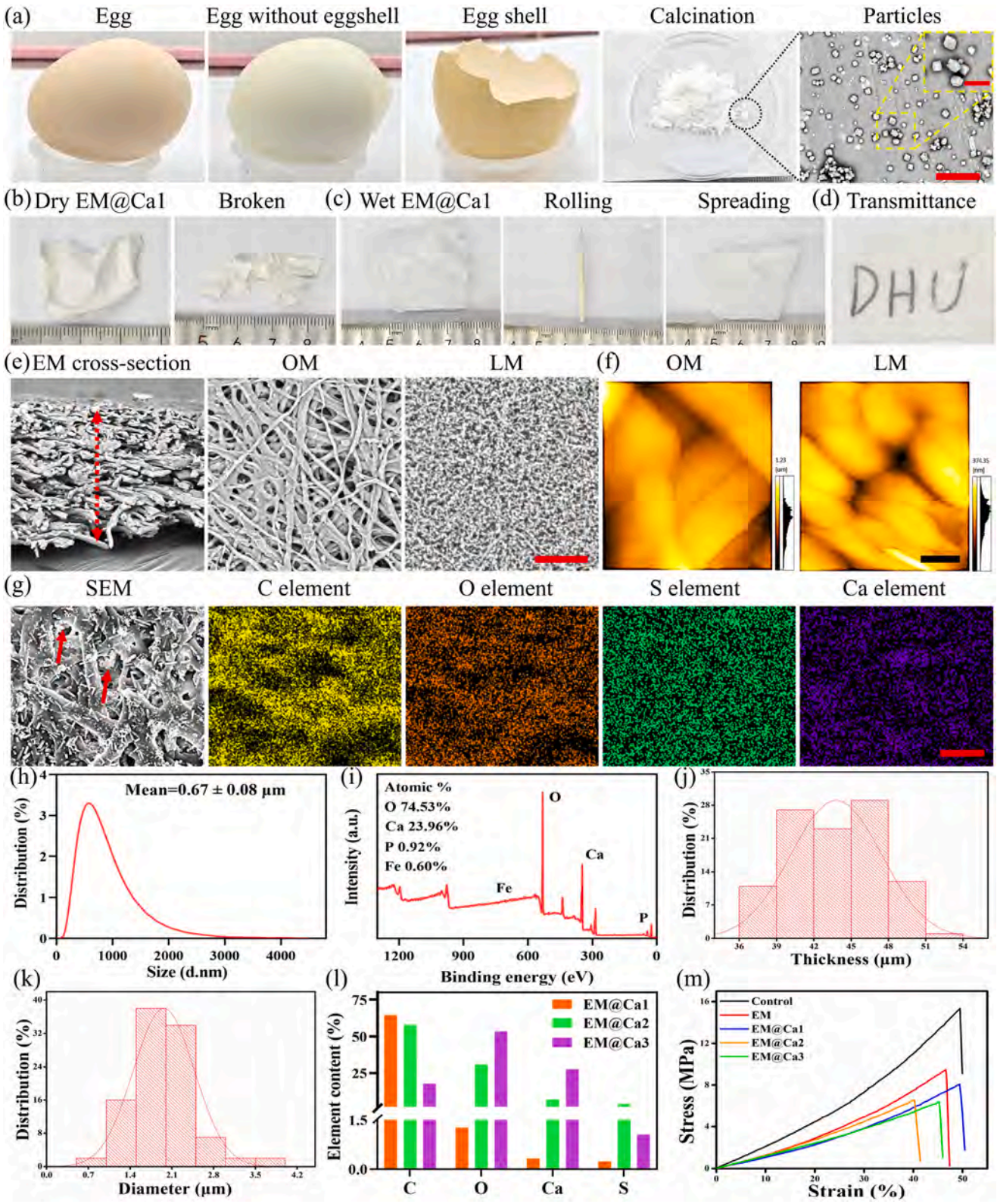

Fig. 4. Illustration as well as characterization of the scaffolds. (a) The macroscopic images of prepared EM and inorganic nanoparticles containing CaO. Scale bars, 3 μm and 10 μm. The morphology of the EM@Ca1 scaffolds in dry state (b) and wet state (c). (d) Light transmittance of EM@Ca1. (e) SEM micrographs and (f) roughness of the EM. Scale bars, 20 μm and 1 μm. (g) SEM and EDS mapping images of EM@Ca1. Scale bars, 6 μm. The red arrows indicate the deposited PCa particles. Size distribution (h) and XPS analysis (i) of PCa. The thickness of EM (j) and fiber diameter of OM (k). (l) Element content of EM@Ca1, EM@Ca2, and EM@Ca3. The representative stress-strain curves (m) of control (UEM), EM, EM@Ca1, EM@Ca2, and EM@Ca3 groups. *P < 0.05, **P < 0.01, and ***P < 0.001. (For interpretation of the references to color in this figure legend, the reader is referred to the Web version of this article.)

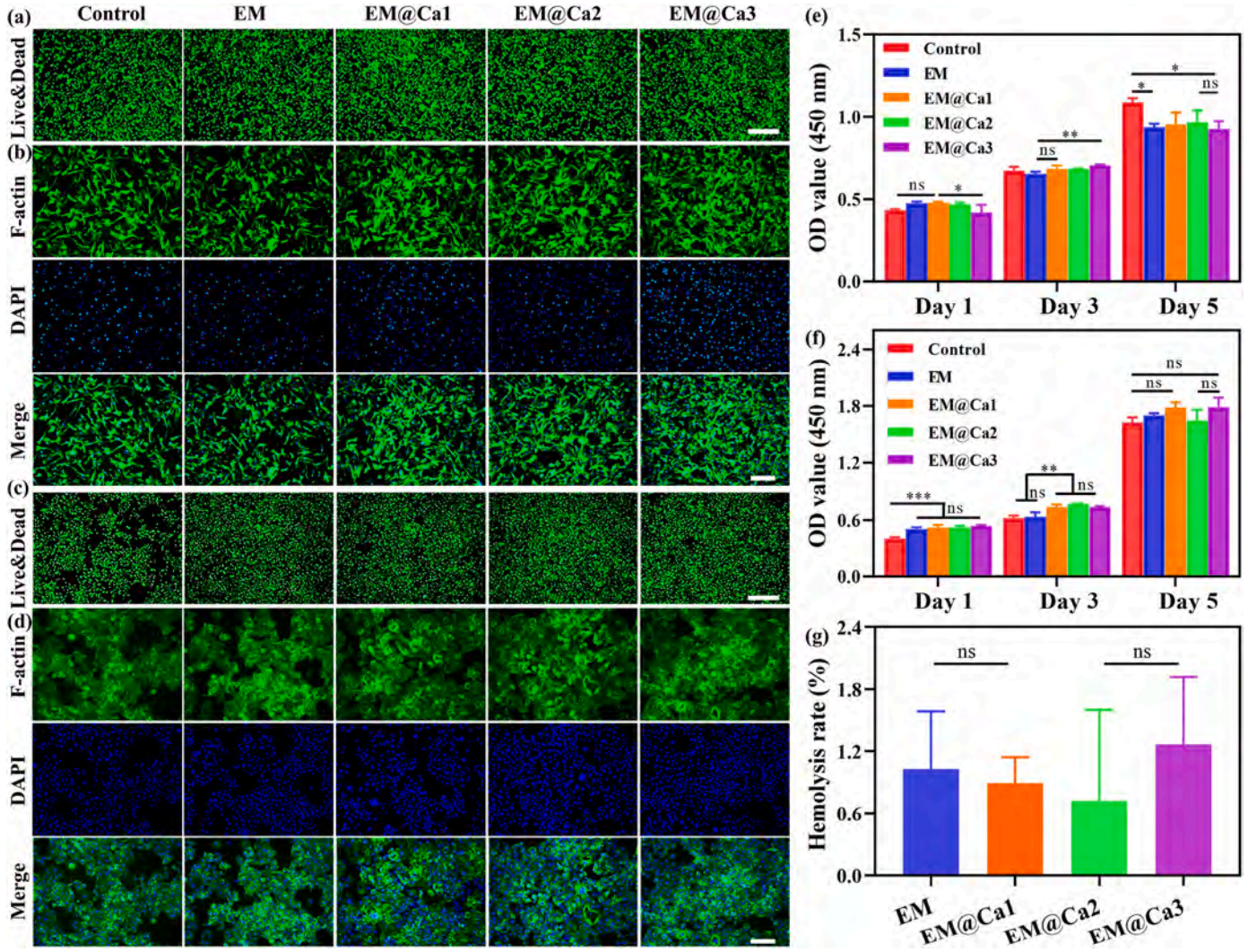

Fig. 5. Biocompatibility of scaffolds *in vitro*. Live/dead staining assay (a) and cell cytoskeleton staining using F-actin (b) of NIH-3T3 fibroblasts cultured along with the extract solution of the control, EM, and EM@Ca scaffolds at day 5. Scale bars, 500 μm and 200 μm. Live/dead staining assay (c), and F-actin staining (d) of HUVECs cultured along with the extract solution of the control, EM, and EM@Ca scaffolds at day 5. Scale bars, 500 μm and 200 μm. Quantitative analysis of the proliferation of NIH-3T3 fibroblasts (e) and HUVECs (f) using CCK-8 assay. Hemolysis rate of scaffolds (g). *P < 0.05, **P < 0.01, and ***P < 0.001.

3.4. Biological function in vitro

To delineate chemotactic as well as angiogenic properties of composite scaffolds, cell migration was studied with a Transwell migration assay and a tube-formation assay using BMSCs and HUVECs *in vitro*. The EM@Ca1, EM@Ca2, and EM@Ca3 scaffolds displayed significant cell migration in comparison to the EM and control groups. The number of migrated cells were 8.7 ± 1.5, 8.67 ± 1.53, 16.7 ± 1.5, 20. ± 2.5, and 35.7 ± 5.1 per HPF (high per field) for BMSCs and 9.0 ± 6.0, 25.3 ± 4.5, 68.0 ± 8.0, 84.3 ± 6.5, and 75.0 ± 7.8 per HPF for HUVECs in control, EM, EM@Ca1, EM@Ca2, and EM@Ca3 groups, respectively. These results manifested that the PCa could promote the migration of BMSCs and HUVECs (Fig. 6a and 6e-f). Moreover, the scratch wound healing assay revealed significant effect of the EM@Ca1, EM@Ca2, and EM@Ca3 groups on the migration of fibroblasts *in vitro* than that of the control and EM groups (Fig. S14, Supporting Information). The EM did not significantly improve cell migration plausibly owing to its poor solubility.

The tube formation assay also revealed significant angiogenic effect of the EM@Ca1, EM@Ca2, and EM@Ca3 scaffolds, which exhibited more number of meshes *in vitro*, thereby indicating the potential of the PCa to promote the angiogenesis (Fig. 6b and g). With the cytocompatibility and biofunction of the composite scaffolds in hand, we next deciphered the osteogenic potential of the scaffolds and delineated the osteogenic differentiation of BMSCs using ALP and ARS assays *in vitro*. EM@Ca1, EM@Ca2, and EM@Ca3 manifested an intense staining both for the ALP and ARS in comparison to the control and EM groups, thereby indicating the osteogenic potential of the PCa *in vitro* (Fig. 6c).

The coagulation properties of the scaffolds were next evaluated (Fig. 6d). The BCI values were found to be 86.8 ± 1.2 %, 85.4 ± 2.3 %, 45.8 ± 2.4 %, 34.4 ± 2.6 %, and 15.9 ± 3.3 % for control, EM, EM@Ca1, EM@Ca2, and EM@Ca3 groups, respectively (Fig. 6h). While control and EM groups manifested poor coagulation (light red color of the testing solution), EM@Ca1, EM@Ca2, and EM@Ca3 groups exhibited significant coagulation properties plausibly due to the calcium ions (Ca^{2+}) (Fig. 6d).

3.5. Biocompatibility of scaffolds in vivo

To discern the biocompatibility of the scaffolds *in vivo*, they were subcutaneously implanted in SD rats for up to 6 weeks (Fig. 7) [24]. H&E staining showed that cells were mainly accumulated at the tissue-scaffold interface with only a limited infiltration into the scaffold. Masson's trichrome (MT) staining showed the lack of collagen deposition in the implanted scaffolds 2 weeks post-implantation (Fig. 7b). With

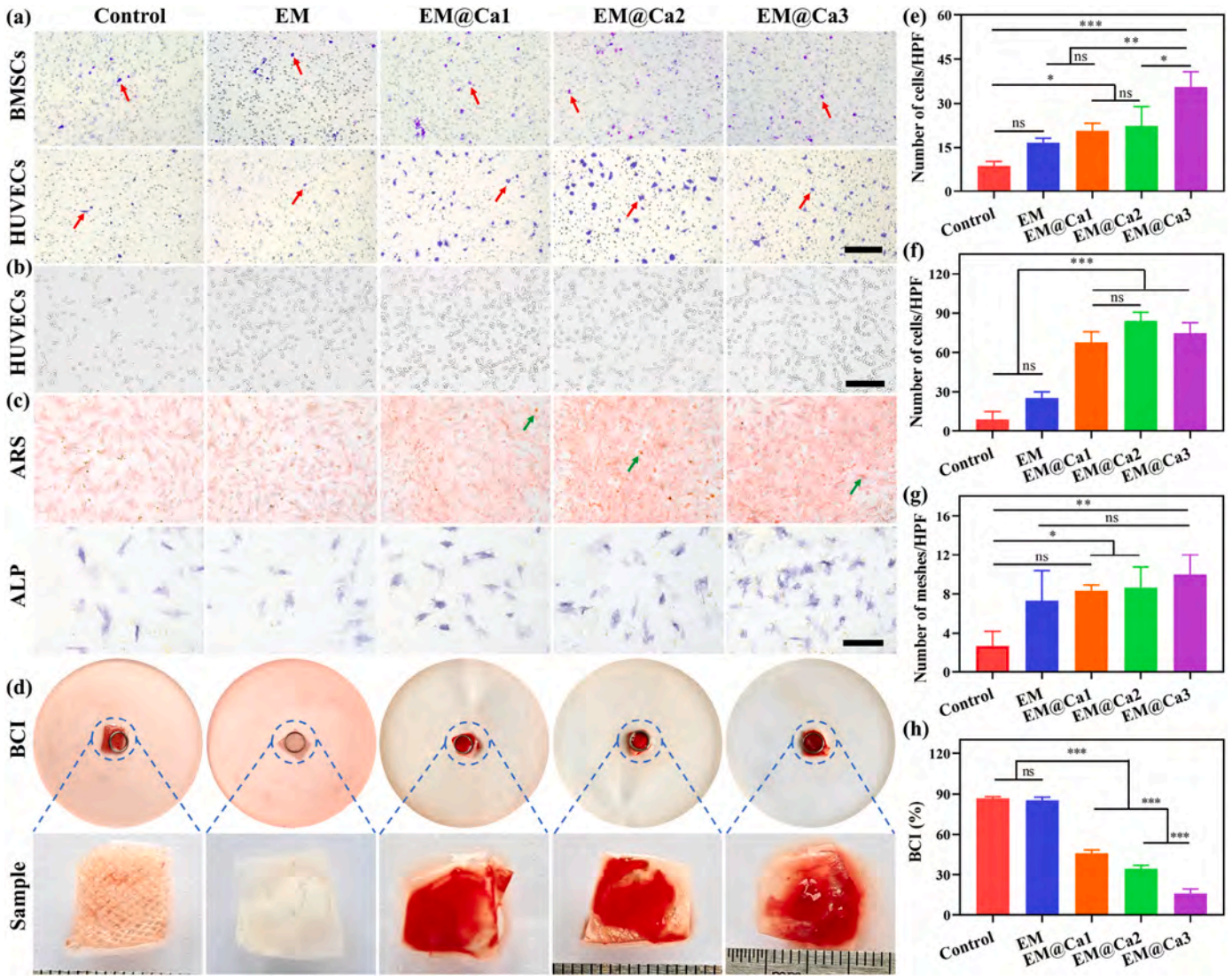

Fig. 6. Biological function of scaffolds *in vitro*. (a) Transwell migration assay of BMSCs and HUVECs. Scale bar, 300 μm. The red arrows point toward migrated cell. (b) Tubule-like network formation of HUVECs *in vitro*. Scale bar, 200 μm. (c) The ARS and ALP staining of BMSCs at day 14. Scale bar, 300 μm. The green arrows indicate the distinct calcium nodules. (d) The macroscopic images of dynamic whole-blood clotting model. Quantitative analysis of BMSCs (e) and HUVECs (f) migrated in a Transwell migration assay. Number of meshes in tube-formation assay (g), and BCI value (h) *in vitro*. *P < 0.05, **P < 0.01, and ***P < 0.001. (For interpretation of the references to color in this figure legend, the reader is referred to the Web version of this article.)

an increase in the implantation time of the scaffolds, cells had gradually infiltrated into the scaffolds albeit only a minute collagen regeneration at 4 weeks (Fig. 7c). By 6 weeks post-implantation, more number of cells were infiltrated into the implanted scaffolds alongside the deposition of the collagen at the scaffolds-tissue interface as well as in the inner side of the scaffolds. It is worthy to note that the number of the recruited cells as well as the extent of the collagen deposition were higher in the composite scaffolds (e.g., EM@Ca1, EM@Ca2, EM@Ca3, etc.) (Fig. 7d). H&E staining of the main organs, including heart, liver, spleen, lung, and kidney did not show an obvious cytotoxicity (Fig. 7e). Taken together, these data indicated that the scaffolds can degrade alongside their infiltration with the host cells and the deposition of collagenous tissues, which may also have implications for their biocompatibility *in vivo*.

3.6. Hemostatic ability of scaffolds in a rabbit liver injury model

The surgical procedures as well as trauma and injury may lead to an uncontrolled bleeding, especially, in the battlefield, thereby causing traumatic incidences and potentially morbidity and mortality [25]. Since the composite scaffolds exhibited significant blood coagulation *in vitro* as revealed with the BCI assay, the hemostatic efficacy of the scaffolds was assessed in a rabbit liver injury model (Fig. 8a). Hemostatic time and blood loss were measured. The control and EM groups had no significant hemostatic effect and showed blood leakage even 45 s after the treatment of the defect (Fig. 8b and c). In contrast, composite scaffolds, including EM@Ca1, EM@Ca2, and EM@Ca3 exhibited a significant hemostatic effect as indicated by the short hemostasis time and the smaller area of blood oozing (Fig. 8d).

3.7. Wound healing in vivo

The ability of the scaffolds to induce skin repair in a full-thickness excisional defect model in SD rats was next evaluated for up to 2 weeks (Fig. 9). Defects treated with EM, EM@Ca1, and EM@Ca3 scaffolds exhibited rapid wound healing rate, which were further facilitated by the transition from the inflammatory phase to the tissue proliferation phase (Fig. 9b). Wounds were gradually healed and only a small wound area was left 14 days post-operatively, especially, in the EM, EM@Ca1 and EM@Ca3 groups, which manifested fast wound healing efficiency (Fig. 9d and e). The EM@Ca1 group exhibited more significant skin

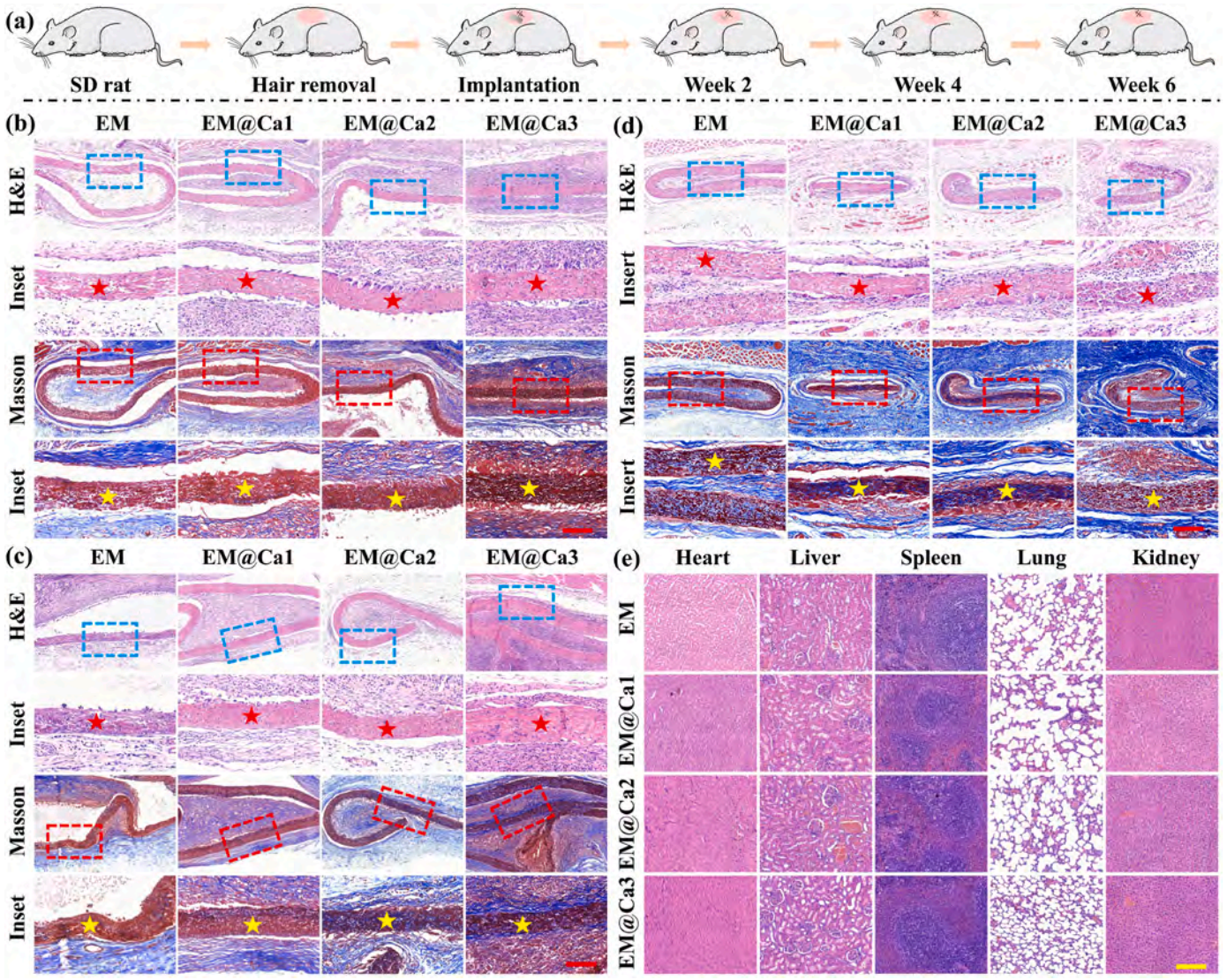

Fig. 7. Biocompatibility of scaffolds in a subcutaneous implantation model. (a) Schematic representation of the implantation of scaffolds in a subcutaneous implantation model in rats. H&E staining and MT staining of scaffolds explanted at 2 weeks (b), 4 weeks (c), 6 weeks (d) post-operatively. Scale bar, 100 μm. The red and yellow pentagrams point toward implanted scaffolds (e) H&E staining of main organs such as heart, liver, spleen, lung and kidney collected from rats implanted with scaffolds for up to 6 weeks. Scale bar, 200 μm. (For interpretation of the references to color in this figure legend, the reader is referred to the Web version of this article.)

repair effect than that of the other groups. EM, EM@Ca1, and EM@Ca3 groups exhibited re-epithelialization compared to that of the control and P-control groups albeit slight inflammation (Fig. 9c and f). MT staining also showed more collagen production alongside skin appendages formation (e.g., hair follicles, sebaceous glands, etc.) in the EM, EM@Ca1, and EM@Ca3 groups at the wound bed (Fig. 9c and g).

3.8. Bone regeneration

Following bone trauma, the healing process may be intervened by the surrounding soft tissues, which may in turn limit the bone repair [26]. As shown in Fig. 10a, the bone defect was created in the tibia, and the scaffolds were implanted on the bone defect site. The CT images revealed a distinct concavity in the defect site in the control group (Fig. 10b). While the thickness of the healed bone defect was similar to the normal tibia in the EM@Ca3 group, defects treated with the control and EM@Ca1 showed porous structure in the bone cross-section (Fig. 10b). The grafts explanted at 6 weeks were subjected to H&E and MT staining (Fig. 10c–d). While *de novo* bone was mainly formed in the center of the defect in the EM@Ca1 and EM@Ca3 groups; the latter exhibited considerable bone formation, which was structurally and morphological similar to that of the normal group. MT staining also showed significantly higher bone formation rate in the EM@Ca3 group as compared to the other groups. The collagen distribution in the EM@Ca3 group was similar to that of the normal group (Fig. 10d). While EM group did not exhibit significant osteo-inductive effect, composite scaffolds (EM@Ca) improved bone tissue regeneration, which may be attributed to the PCa. Taken together, the EM@Ca3 scaffold may promote bone formation alongside isolating the bone from the surrounding soft tissues.

4. Discussion

Conventional scaffolds used for soft and hard tissue repair include hydrogels, aerogels and other application forms, which usually require natural and synthetic polymers alongside crosslinkers and complex preparation process [27]. Therefore, it is imperative to fabricate TE scaffolds by leveraging alternative scaffold materials as well as

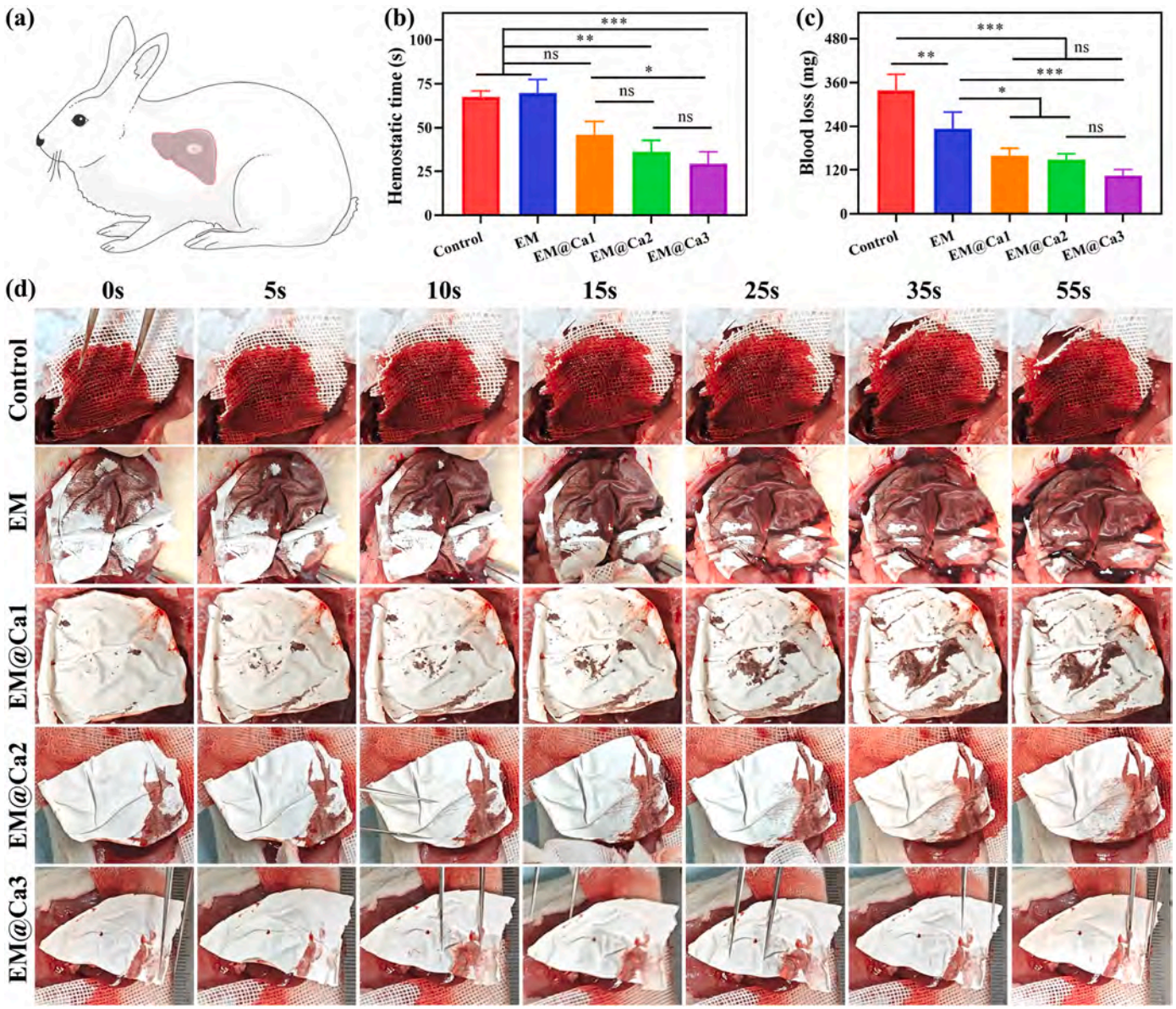

Fig. 8. Hemostatic ability of scaffolds *in vivo*. (a) Schematic diagram showing the hemostatic ability of scaffolds in a rabbit liver trauma injury model. Quantitative analysis of hemostatic time (b), and blood loss (c). Photographs showing the treatment of liver blood with various scaffolds for up to 0, 5, 10, 15, 25, 35, 55 s after injury (d). *P < 0.05, **P < 0.01, and ***P < 0.001.

modification approaches. We have exploited EM and PCa particles derived from the ES to design composite scaffolds alongside their potential utility for the soft and hard tissue repair. We performed in-depth metabolomics and proteomics studies of the EM with or without heat treatment to gain an insight into their multifunctional characteristics for the wound healing and bone regeneration. Metabolomics analysis showed different types of bioactive components in the EM. The top 20 substances from EM untargeted metabolomics analysis were further subjected to the network pharmacology analysis with respect to the wound healing and bone repair (Fig. 2). The GO function enrichment analysis showed that the key targets for the wound healing and bone repair were MMP9, MAPK3, IL-1B, IL-6, TNF, HIF1A, EGFR, TP53, TGF-β1, and so on (Fig. 3c). These cytokines and chemokines can modulate several biofunctions, such as inflammation, microbial infection, cell growth and differentiation, etc., thereby indicating potential anti-inflammatory effects of the EM [28]. The network pharmacology analysis of KEGG enrichment indicated that the EM could activate related signaling pathways to accelerate the formation of *de novo* blood vessels, regulate inflammatory microenvironment of the regenerated tissues, and promote cell growth at the defect site, which may have implications for the potential utilization of the EM as a scaffold for TE applications (Fig. 3d and f).

The EM is a semi-permeable double-layered porous membrane, which is rich in collagen-based fibrous matrix between the ES and egg white. The EM tightly interacts with the ES via complex transitional structure; mammillary knobs are integrated into the mineral mammillary columns to enable a cohesive structure (Fig. 4e) [9]. Nevertheless, intact pieces of the EM are tedious to be isolated [29]. We prepared intact purified EM with sufficent structural integrity (Fig. 4a). The EM and ES are closely connected to enable an integrated structure with distinct mechanics. On the other hand, the ES contains several inorganic components, including $CaCO_3$ albeit its poor biofunction for the regenerative medicine and TE. Since the EM may have the components not conducive for the TE, we heat-treated the EM to avoid these components while retaining flexibility and ECM-like microstructure of the EM. We calcined ES to fabricate PCa particles; the latter may retain the high

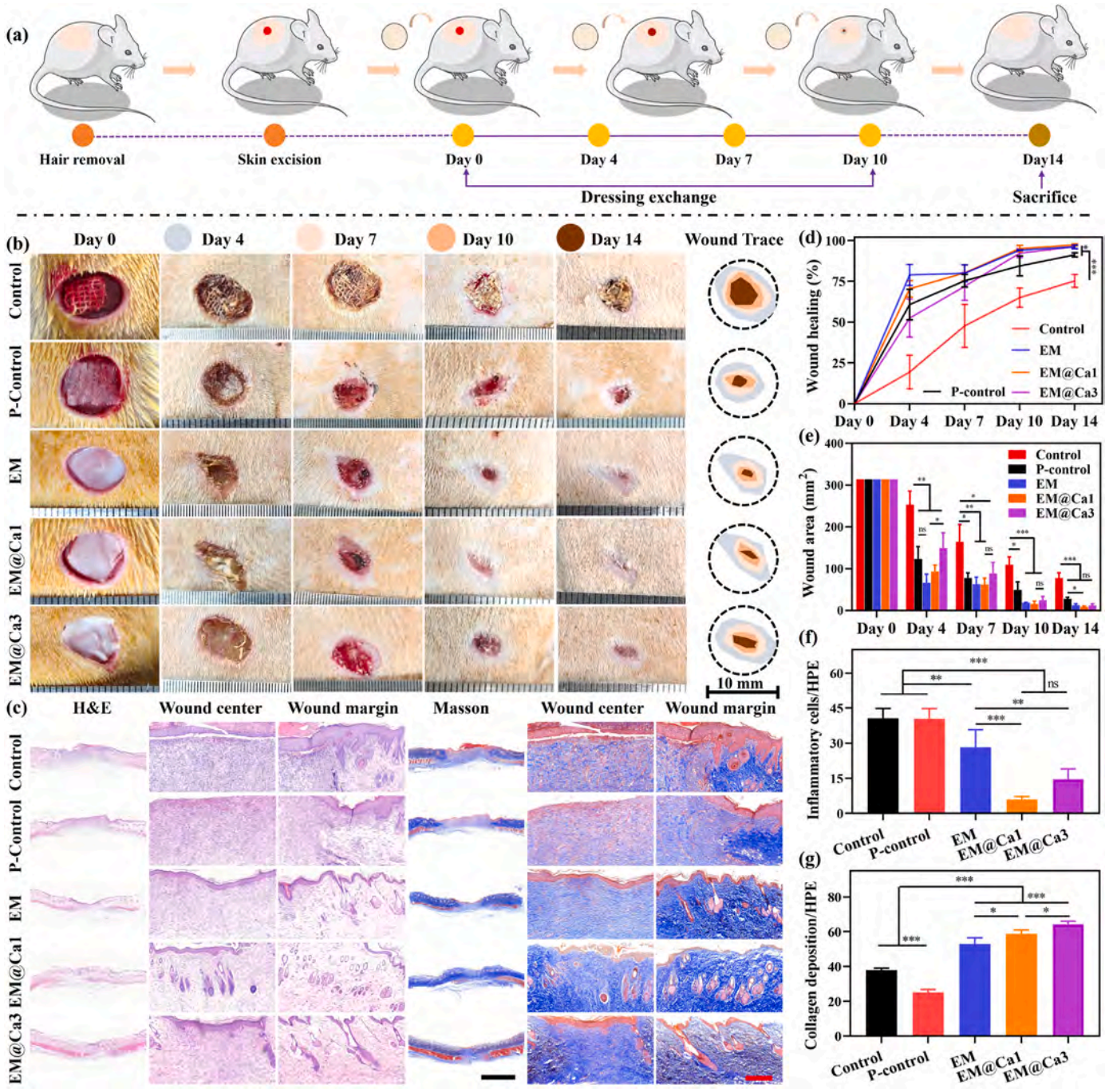

Fig. 9. Evaluation of scaffolds for skin repair in a full-thickness excisional defect model in SD rats. (a) Schematic diagram showing the implantation of membranes. The dressings were exchanged at an interval of 3 days and rats were sacrificed at day 14 post-operatively. (b) Representative images of wound area and closure trace of wounds by day 14. (c) H&E staining and MT staining of wound center and margins at day 14. Scale bars, 3 mm and 300 μm. (d) Wound area at each time point normalized with respect to day 0, and the percentage wound closure rate at day 14. The number of inflammatory cells (f) and collagen deposition (g) in wound site at day 14. *P < 0.05, **P < 0.01, and ***P < 0.001.

specific surface area for an easier incorporation into the scaffold materials alongside the incorporation of the bioactive components to facilitate tissue repair. We envision that the combination of the EM and PCa could enable the transformation of waste resources into biologically active scaffolds for TE applications. Consequently, the composite scaffolds based on EM and PCa may be more beneficial than that of the utilization of ES.

The OM exhibits rough porous structure, which provides anchoring sites to the tips of the calcified ES (Fig. 4e). The smooth surface texture lies between the OM and LM with pore size in the range of 5–15 μm and is essential for the diffusion of oxygen and the transport of the water. On the other hand, LM is composed of the compact bundled fiber particles and forms smooth membrane surface to prevent the leakage of the egg white (Fig. 4e) [5,30]. The average thickness of the EM was *ca.* 50 μm, while that of the LM was *ca.* 0.5–1% of the total EM thickness (Fig. 4e). The thickness of the inner and outer membranes was 20–30 % and 70–80 %, respectively (Fig. 4e) [8]. The EM, especially, positioning toward the IM side possesses an interwoven fibrous structure and has been widely utilized as a scaffolds and shown to serve as a barrier to restrict the moisture loss alongside the invasion of the pathogens [8].

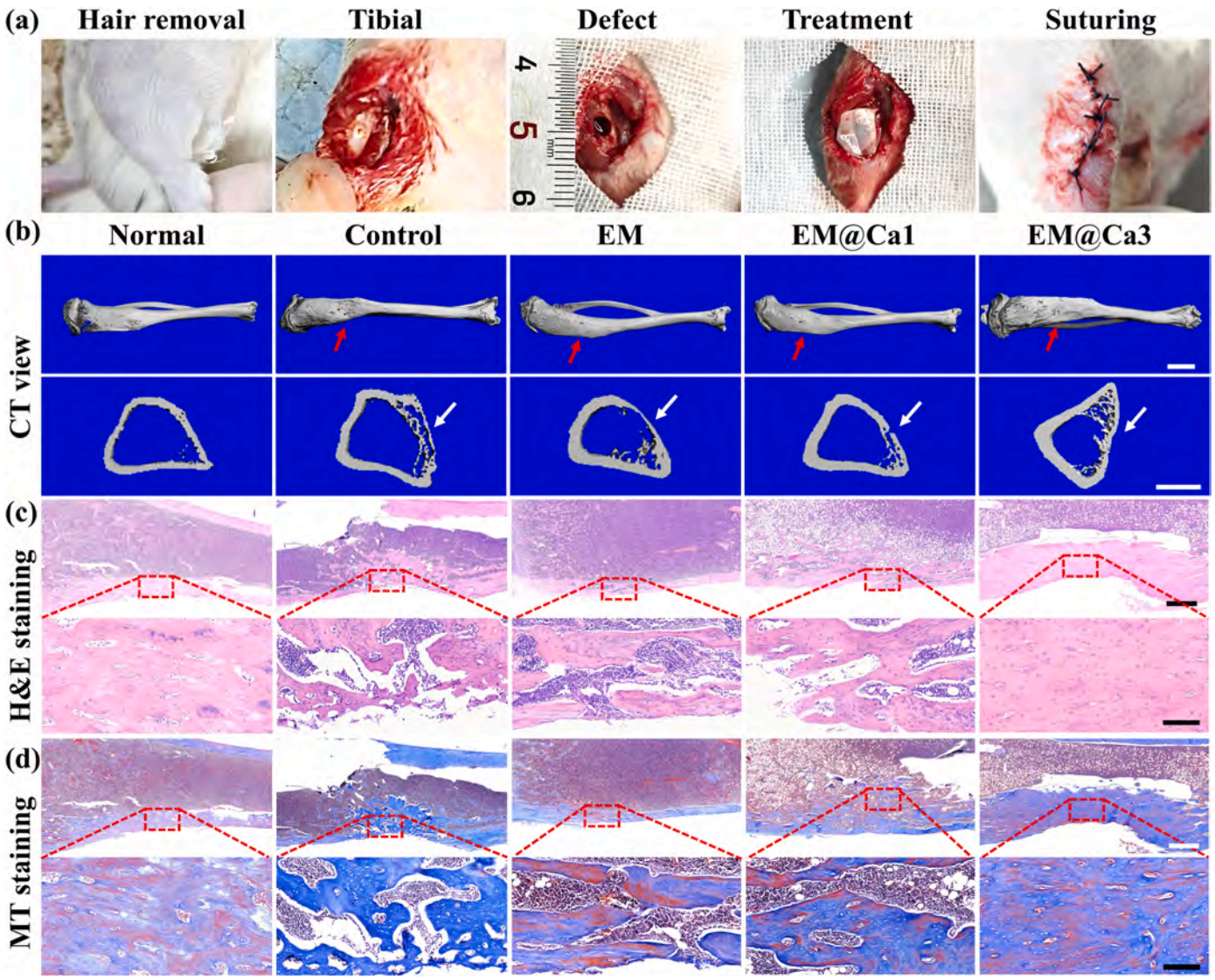

Fig. 10. The bone regeneration by using different scaffolds. (a) Preparation of bone defect model and its treatment process of bone defects. (b) 3D reconstructed micro-CT images of femoral after 6 weeks. Scale bars, 5 mm and 2 mm. Histological observation of new bone formation at bone defect areas after various scaffold treatment by (c) H&E and (d) MT staining at 6 weeks. Scale bars, 1 mm and 150 μm.

Interestingly, the EM has been processed into various application forms, including raw, autoclaved, and powdered [31]. The UEM and EM showed different ingredients as revealed by the metabolomics (Figs. S3 and S4, Supporting Information) [8,32]. While the UEM may pose adverse effects for cell proliferation, the heat-treated EM may overcome these limitations [32,33]. The EM also possesses thermal stability and degradation-resistance alongside good cell attachment efficiency than that of the raw UEM [33].

The EM exhibited different types of bioactive molecules, including collagens, HA, and proteins; these components may be conducive to maintain the fibrous structure of the EM as well as impart viscoelastic characteristics to the scaffold [8]. The EM fiber manifested a core rich in collagen surrounded by a fuzzy glycoproteic mantle in the microstructure [8,32]. The EM is composed of 80–85 % of the inorganic content (e.g., C, 36–47.5 %; H, 5–6.8 %; N, 11–15.3 %; O, 12.0 %; and S, 2–3.0 %, etc.), structural proteins (e.g., keratin, laminin, agrin, ovoglycan, desmozine, isodesmozine, ovoglycoprotein, ovocalyxin-36, etc.), collagen (type I, V, and X), and cysteine-rich eggshell membrane proteins (CREMPs). The composition of the EM was found to be similar to that of human ECM [32,34]. The CREMPs forms disulfide linkages between EM fibers to enhance the structural strength with highly stability and insoluble performance [33].

The ES manifestedshowed brittle and fragile behavior, which may be ascribed to the inorganic components including Ca and P [35]. The ES powder has been widely used as a source of inorganic components for both soft and hard tissue repair owing the ability of the Ca to promote biomineralization and wound healing [14]. The hydroxyapatite derived from the ES mirrors structural components of the hard tissues alongside good cytocompatibility for osteoblasts alongside its ability to promote bone ingrowth and resorption [32]. However, owing to the presence of the $CaCO_3$ and protein fibers, the ES exhibits a high degree of hardness, which renders it difficult to be directly employed as a scaffold for TE [36,37].

Inorganic bioactive material, such as bioactive glass (BG) and hydroxyapatite are widely used for soft and hard tissue repair, thanks to their abilities to promote angiogenesis, collagen deposition, cell proliferation, hemostasis, and other functions [16]. The ES could be calcined to prepare the PCa particles, which may contain different types of inorganic components, including calcium oxide (CaO) and phosphorous pentaoxide (P_2O_5), thereby resembling the structure and composition of the BG. The PCa particles may furnish therapeutic ions to promote ECM deposition, angiogenesis and biomineralization [19,38]. However, the

direct use of the PCa particles may increase the pH at the injury site alongside posing potential toxicity risks owing to their ability to interact with the water due to a polar surface; the latter may also lead to the fast release of the therapeutic ions [16,39].

While the OM side of the EM exhibited pore size distribution in the range of 5–15 μm, the IM side of the EM displayed thin yet a dense smooth surface, with an overall thickness of *ca.* 50 μm (Fig. 4j). Therefore, the EM with good structural and mechanical properties may be exploited as a 3D scaffolds with a single-sided microporous structure similar to the Janus structure [40]. The average size of the PCa particles was found to be *ca.* 0.67 μm, which were incorporated into the pores of the EM to afford EM@Cax scaffolds; the *x* denotes the content of the PCa particles. The incorporation of the PCa particles into the EM may be beneficial to improve the biocompatibility as well as biological function of the scaffolds (Fig. 5).

The EM@Cax scaffolds (e.g., EM@Ca1, EM@Ca2, EM@Ca3, etc.) manifested good biocompatibility and biological functions as revealed by the negligible hemolysis ratio, good cell viability alongside continuous cell proliferation, for both NIH-3T3 fibroblasts and HUVECs (Fig. 5e and f). The composite scaffolds enabled cell migration, *de novo* production of capillaries from HUVECs, and blood coagulation *in vitro* (Fig. 6d). The ALP and ARS staining further revealed osteo-inductive potential of BMSCs *in vitro*, thereby indicating their regenerative potential both for the soft and hard tissues (Fig. 6c) [39,41].

Since inorganic nanomaterials may induce toxic effects owing to their size, shape, surface charge, stability, and concentration, it is also imperative to delineate the biocompatibility of the composite scaffolds *in vivo* [42]. The PCa particles could release therapeutic ions, such as calcium ions (Ca^{2+}) and magnesium ions (Mg^{2+}), which may plausibly accumulate at the injury site, thereby increasing the pH, both at the injury site as well as the surrounding tissues [16,39]. Therefore, we preliminary discerned the biocompatibility of the composite scaffolds in a subcutaneous implantation model in rats, wherein they enabled cellular infiltration from the host tissues alongside the production of ECM without an obvious cytotoxicity to the most of the organs [43]. The composite scaffolds also displayed a longer degradation period, which may limit the biological function of EM components (Fig. 7d) [44].

Since artificial synthetic polymers may induce acidic degradation products at the injury site and potentially induce inflammation, they generally require the incorporation of the bioactive components including gelatin and silk fibroin (SF) to regulate the degradation behavior. In contrast, the degradation products of the EM@Ca1 and EM@Ca3 scaffolds are most likely composed of the peptides and amino acids, which may be safer as compared to the acidic degradation products of the most of the artificial synthetic implant materials used for the soft and hard tissue repair. The proteinase K can promote the degradation of natural proteins and therefore it can be used to treat EM to realize the regulation of the degradation rate of EM in follow-up studies [45].

The EM@Cax also exhibited rapid hemostatic ability in a rabbit liver trauma model plausibly due to the good water uptake ability of the scaffolds, which may ensure rapid blood absorption to form wet adhesion and physical barriers to prevent further bleeding (Fig. 8d). These composite scaffolds can additionally furnish therapeutic ions including calcium ions (Ca^{2+}) and magnesium ions (Mg^{2+}), which may also mediate intrinsic and extrinsic coagulation pathways and affect hemostatic ability by augmenting platelet activation and aggregation by the protein kinase C (PKC). The EM with the porous structure alongside its fibers may also absorb red blood cells (RBCs) and platelets and accelerate blood coagulation (Fig. 6d) [46,47].

Wound healing involves a series of overlapping cellular events, such as hemostasis, inflammation, proliferation, and remodeling [48,49]. Traditional dressings exhibit air permeability and superior hemostatic performance albeit their ability to induce tissue adhesion at the injury site and the additional difficulty to obscure the wound monitoring [16]. On the other hand, hydrogel dressings could form a wet healing microenvironment to accelerate skin repair albeit their poor hemostatic performance, poor wound management in the humid environment microenvironment, and recurrence of infection and inflammation [50,51]. Thus, the composite scaffolds were further evaluated in a full-thickness excisional defect modal in the rats, which manifested their ability to promote the skin repair alongside the formation of epithelial cell layer, cell proliferation, wound contraction, angiogenesis, and regulation of the inflammatory microenvironment.

Good wound healing ability of the composite scaffolds may be ascribed to various factors. First, the EM could suppress oxidative stress and inflammation level at the wound site [52]. The solubilized EM using enzymatic hydrolysis has indeed been shown to promote anti-oxidative abilities by scavenging free radicals as well as preventing DNA damage [8]. Second, the EM could down-regulate the expression level of the inflammatory cytokines plausibly via nuclear factor Kappa light chain-activator (NFkB) pro-inflammatory pathway and other immunomodulatory effects on macrophages and monocytes by reducing the activity of the NF-kB, TLR-4 (toll-like receptor 4) and ICAM-1 (intercellular cell adhesion molecule-1) at mRNA transcription levels [8]. Third, the small pore size of the EM may help suppress bacterial infection [53].

We further observed the considerable promise of the EM@Ca3 scaffolds to promote bone regeneration in comparison to the defect only or the EM-treated defects. The tibial defects treated with EM@Ca3 manifested higher thickness of healed bone layer, less number of inflammatory cells, and dense bone matrix tissue form as compared to the defect only or EM groups. The significant bone tissue repair by the EM@Ca3 composite scaffolds is ascribed to their osteo-inductive, angiogenic, and therapeutic ion release effect. Therapeutic ions including calcium ions (Ca^{2+}) and phosphate ions (PO_4^{3-}) from the PCa particles may further play an important role to promote the tissue repair alongside their ability to influence the expression of vascular endothelial growth factor (VEGF) in HUVECs; the latter may further facilitate tissue repair [54,55]. Therapeutic ions could further promote cell attachment, growth, and osteo-genesis by regulating the FAK/JNK/p38 signaling pathways [56].

The bioactive component of the EM may also regulate the inflammation microenvironment at the injury site to enhance matrix maturation as well as mineralization [27]. As compared to the bone cement or hydrogel scaffolds, which are often used for the fracture repair, the composite scaffolds can not be directly filled in the bone defect and can avoid inflammation at the bone defect site. The release of bioactive components from the scaffold can promote the migration of the surrounding tissues of the bone defect site for bone repair plausibly even under an incomplete degradation of the scaffold. Moreover, the EM may also effectively isolate the bone defect site from the surrounding soft tissues, thereby avoiding an interference of the soft tissues to impair bone repair [57].

To put together, the ES were formulated into TE scaffolds by uniquely leveraging various methods alongside an effective utilization of otherwise waste resources into useful biomedical materials [13]. Composite scaffolds manifested potential usefulness characteristics for both the skin and bone repair; flexibility and transparency of scaffolds may enable appropriate wound management [54,58]. On the other hand, scaffolds exhibited Janus-like structure; the LM suppress the adhesion of surrounding tissues while the OM surface may furnish bioactive cues at the defect site for bone tissue repair [59].

This study has also some limitations. These scaffolds exhibit longer degradation period owing to the highly cross-linked structure and poorly soluble properties, which may constrict the release of active ingredients. Similarly, unlike the traditional 3D scaffolds, these composite scaffolds possessed relatively thinner structure (ca. 50 μm), which may limit their applicability and necessitates further optimization.

5. Conclusion

The EM and ES are cost-effective, which can be conducive to promote

skin and bone tissue regeneration. We have successfully fabricated composite scaffolds based on the EM and PCa particles to afford different types of EM@Cax scaffolds with the varying content of the PCa particles. The composite scaffolds exhibited porous structure as well as manifested biocompatibility and biological functions *in vitro*. The composite scaffolds also promoted the infiltration of host cells in a subcutaneous implantation model and encouraged bone regeneration *in vivo*. Taken together, these cost-effective yet multifunctional composite scaffolds composed of the green components may hold great promise for the regeneration of soft and hard tissues and may also be worthy for the other related disciplines.

CRediT authorship contribution statement

Zhengchao Yuan: Writing – original draft, Validation, Investigation, Funding acquisition, Data curation. **Siyuan Wu:** Visualization, Software, Project administration, Formal analysis. **Liwen Fu:** Software, Resources, Investigation, Data curation. **Muhammad Shafiq:** Writing – review & editing, Writing – original draft, Visualization, Validation, Resources, Investigation, Formal analysis, Data curation. **Yuqing Liang:** Validation, Supervision, Methodology, Formal analysis. **Peng Li:** Visualization, Software, Methodology, Formal analysis. **Xinyi Wang:** Software, Methodology, Data curation. **Hao Feng:** Validation, Methodology, Formal analysis, Data curation. **Rashida Hashim:** Writing – review & editing, Visualization, Software, Methodology. **Shuqi Lou:** Methodology, Conceptualization. **Mohamed EL-Newehy:** Software, Funding acquisition, Formal analysis, Conceptualization. **Meera Moydeen Abdulhameed:** Validation, Resources, Methodology, Data curation. **Weifen Zhang:** Writing – review & editing, Visualization, Funding acquisition, Data curation. **Xiumei Mo:** Writing – review & editing, Supervision, Resources, Project administration, Funding acquisition, Data curation, Conceptualization. **Shichao Jiang:** Writing – review & editing, Supervision, Project administration, Methodology, Funding acquisition.

Declaration of competing interest

The authors declare that they have no known competing financial interests or personal relationships that could have appeared to influence the work reported in this paper.

Acknowledgments

This work was supported by the Major Innovation and Technology Engineering Project of Shandong Province (2019JZZY011106), Science and Technology Commission of Shanghai Municipality, China (20DZ2254900), Sino German Science Foundation Research Exchange Center, China (M – 0263), and China Education Association for International Exchange (2022181). This research was also supported by the Taishan Scholars Program of Shandong Province (tsqn201812141), Shandong Provincial Natural Science Foundation (ZR2021MH004, ZR2022QH063), and China Postdoctoral Science Foundation (2023M742325). This project was also supported by Researchers Supporting Project Number (RSP2024R65), King Saud University, Riyadh, Saudi Arabia, and the Fundamental Research Funds for the Central Universities and Graduate Student Innovation Fund of Donghua University (CUSF-DH-D-2024040).

Appendix A. Supplementary data

Supplementary data to this article can be found online at https://doi.org/10.1016/j.compositesb.2024.112071.

Data availability

Data will be made available on request.

References

[1] Hong C, Chung H, Lee G, Kim C, Kim D, Oh SJ, et al. Hydrogel/nanofiber composite wound dressing optimized for skin layer regeneration through the mechanotransduction-based microcellular environment. ACS Appl Bio Mater 2023; 6:1774–86.
[2] Liu X, Gaihre B, Li L, Rezaei A, Tilton M, Elder BD, et al. Bioorthogonal "click chemistry" bone cement with bioinspired natural mimicking microstructures for bone repair. ACS Biomater Sci Eng 2023;9:1585–97.
[3] Wei YJ, Chen H, Zhou ZW, Liu CX, Cai CX, Li J, et al. Kill two birds with one stone: dual-metal MOF-nanozyme-decorated hydrogels with ROS-scavenging, oxygen-generating, and antibacterial abilities for accelerating infected diabetic wound healing. Small 2024;2403679:1–17.
[4] Asadi N, Sadeghzadeh H, Rahmani Del Bakhshayesh A, Nezami Asl A, Dadashpour M, Karimi Hajishoreh N, et al. Preparation and characterization of propolis reinforced eggshell membrane/GelMA composite hydrogel for biomedical applications. BMC Biotechnol 2023;23(1):1–12.
[5] Wu S, Yuan Z, Xie P, Shafiq M, Hou J, Liang Y, et al. Lecithin-complexed oregano essential oil-encapsulated fibrous barriers prevent postoperative adhesions by regulating Nrf2/NF- κ B signaling pathways. Appl Mater Today 2024;38:102185.
[6] Chen X, Chen Y, Fu B, Li K, Huang D, Zheng C, et al. Eggshell membrane-mimicking multifunctional nanofiber for in-situ skin wound healing. Int J Biol Macromol 2022;210:139–51.
[7] Hu L, Song C, Li H, Gao Y, Zhang J, Gao T, et al. Oxidized dextran/chitosan hydrogel engineered with tetrasulfide-bridged silica nanoparticles for postsurgical treatment. Macromol Biosci 2023;24(1):2200565.
[8] Pillai MM, Saha R, Tayalia P. Avian eggshell membrane as a material for tissue engineering: a review. J Mater Sci 2023;58:6865–86.
[9] Torres-Mansilla A, Hincke M, Voltes A, López-Ruiz E, Baldión PA, Marchal JA, et al. Eggshell membrane as a biomaterial for bone regeneration. Polymers 2023;15: 1342–70.
[10] Mensah RA, Jo SB, Kim H, Park S-M, Patel KD, Cho KJ, et al. The eggshell membrane: a potential biomaterial for corneal wound healing. J Biomater Appl 2021;36:912–29.
[11] Mensah RA, Cook MT, Kirton SB, Hutter V, Chau DYS. A drug-incorporated-microparticle-eggshell-membrane-scaffold (DIMES) dressing: a novel biomaterial for localised wound regeneration. Eur J Pharm Biopharm 2023;190:258–69.
[12] Saha R, Patkar S, Maniar D, Pillai MM, Tayalia P. A bilayered skin substitute developed using an eggshell membrane crosslinked gelatin-chitosan cryogel. Biomater Sci 2021;9:7921–33.
[13] Liu W, Tang C, Cai Z, Jin Y, Ahn DU, Huang X. The effectiveness of polypeptides from phosvitin and eggshell membrane in enhancing the bioavailability of eggshell powder calcium and its accumulation in bones. Food Biosci 2023;51:102257.
[14] Kongpaopong K, Ratchatawatanapipat N, Tangboriboon N. Bio-cellular glass–ceramic composite with embedded calcium phosphate from eggshell for alternative biomaterials in medical and dental applications. J Appl Polym Sci 2021; 138(20):138459.
[15] Alacam S, Timur S, Telefoncu A. A novel biosensor based on L-homocysteine desulfhydrase enzyme immobilized in eggshell membrane. J Mol Catal B Enzym 2007;49:55–60.
[16] Yuan Z, Zhang L, Jiang S, Sha M, Cai Y, Chen Y, et al. Anti-inflammatory, antibacterial, and antioxidative bioactive glass-based nanofibrous dressing enables scarless wound healing. Smart Mater Med 2023;4:407–26.
[17] Wang C, Yang M, Chen L, Stehle Y, Lin M, Zhang R, et al. Polycaprolactone strengthening gelatin/nano-hydroxyapatite composite biomaterial inks for potential application in extrusion-based 3D printing bone scaffolds. Collagen and Leather 2024;6:27–49.
[18] Abdelrazig S, Safo L, Rance GA, Fay MW, Theodosiou E, Topham PD, et al. Metabolic characterisation of magnetospirillum gryphiswaldense MSR-1 using LC-MS-based metabolite profiling. RSC Adv 2020;10:32548–60.
[19] Song Z, Yu H, Hou L, Dong Y, Hu M, Wei P, et al. Mechanics-resilient HA/SIS-based composite scaffolds with ROS-scavenging and bacteria-resistant capacity to address infected bone regeneration. Adv Funct Mater 2024;24(34):2315382.
[20] Deng W, Zhang W, He Q. Study on the mechanism of puerarin against osteoarthritis from ferroptosis based on network pharmacology and bioinformatics. Naunyn-Schmiedeberg's Arch Pharmacol 2024;397:959–68.
[21] Rasmussen JA, Villumsen KR, Ernst M, Hansen M, Forberg T, Gopalakrishnan S, et al. A multi-omics approach unravels metagenomic and metabolic alterations of a probiotic and synbiotic additive in rainbow trout. Microbiome 2022;10:1–19.
[22] Chai Z, Li Y, Liu F, Du B, Jiao T, Zhang C, et al. Outer eggshell membrane as delivery vehicle for polysaccharide/protein microcapsules incorporated with vitamin e. J Agric Food Chem 2013;61:589–95.
[23] Yuan Z, Shafiq M, Zheng H, Zhang L, Wang Z, Yu X, et al. Multi-functional fibrous dressings for infectious injury treatment with anti-adhesion wound healing. Mater Des 2023;235:112459.
[24] Lei K, Wang K, Sun Y, Zheng Z, Wang X. Rapid-fabricated and recoverable dual-network hydrogel with inherently anti-bacterial abilities for potential adhesive dressings. Adv Funct Mater 2021;31:2008010.
[25] Lin D, Li M, Wang L, Cheng J, Yang Y, Wang H, et al. Multifunctional hydrogel based on silk fibroin promotes tissue repair and regeneration. Adv Funct Mater 2024;34:2405255.
[26] Selvaraj S, Chauhan A, Radhakrishnan A, Rana G, Dutta V, Batoo KM, et al. Cerium oxide nanoparticles and their polymeric composites: advancements in biomedical applications. J Inorg Organomet Polym Mater 2024. https://doi.org/10.1007/s10904-024-03263-5.

[27] Wang X, Yuan Z, Shafiq M, Cai G, Lei Z, Lu Y, et al. Composite aerogel scaffolds containing flexible silica nanofiber and tricalcium phosphate enable skin regeneration. ACS Appl Mater Interfaces 2024;16:25843–55.
[28] Cao G, Liu J, Liu H, Chen X, Yu N, Li X, et al. Integration of network pharmacology and molecular docking to analyse the mechanism of action of oregano essential oil in the treatment of bovine mastitis. Vet Sci 2023;10:350–63.
[29] Bessashia W, Berredjem Y, Hattab Z, Bououdina M. Removal of basic fuchsin from water by using mussel powdered eggshell membrane as novel bioadsorbent: equilibrium, kinetics, and thermodynamic studies. Environ Res 2020;186:109484.
[30] Sun B, Wu T, Wang J, Li D, Wang J, Gao Q, et al. Polypyrrole-coated poly(l-lactic acid-co-ε-caprolactone)/silk fibroin nanofibrous nerve guidance conduit induced nerve regeneration in rat. J Mater Chem B 2016;4:6670–9.
[31] Jia J, Duan YY, Yu J, Lu JW. Preparation and immobilization of soluble eggshell membrane protein on the electrospun nanofibers to enhance cell adhesion and growth. J Biomed Mater Res, Part A 2008;86:364–73.
[32] Sah MK, Rath SN. Soluble eggshell membrane: a natural protein to improve the properties of biomaterials used for tissue engineering applications. Mater Sci Eng C 2016;67:807–21.
[33] Shi Y, Zhou K, Li D, Guyonnet V, Hincke MT, Mine Y. Avian eggshell membrane as a novel biomaterial: a review. Foods 2021;10:1–15.
[34] Lian S, Mu Z, Yuan Z, Shafiq M, Mo X, Mu W. Methacrylated gelatin and Platelet-Rich plasma based hydrogels promote regeneration of Critical-Sized bone defects. Regen Biomater 2024;11:rbae022.
[35] Been S, Choi J, Cho H, Jeon G, Song JE, Bucciarelli A, et al. Preparation and characterization of a soluble eggshell membrane/agarose composite scaffold with possible applications in cartilage regeneration. J Tissue Eng Regen Med 2021;15:375–87.
[36] Li J, Zhai D, Lv F, Yu Q, Ma H, Yin J, et al. Preparation of copper-containing bioactive glass/eggshell membrane nanocomposites for improving angiogenesis, antibacterial activity and wound healing. Acta Biomater 2016;36:254–66.
[37] Ming Z, Han L, Zhu H, Bao M, Fan Q, Xue S, et al. An injectable antibacterial hydrogel to regulate ocular immune for endophthalmitis treatment. Chem Eng J 2023;465:142889.
[38] Lee S, Kang J Il, Kim Y, Park KM. Oxygen-generating tissue adhesives via CaO2-mediated oxygen generation and in situ catechol oxidation for wound management. Composites Part B 2023;266:110951.
[39] Yuan Z, Zhang L, Zheng H, Shafiq M, Song J. The ZnO-based fibrous poly (L-lactide-co-glycolide)/gelatin dressings enable rapid hemostasis and skin regeneration in an infectious wound model. J Drug Deliv Sci Technol 2023;89:105072.
[40] Cui C, Wu T, Chen X, Liu Y, Li Y, Xu Z, et al. A Janus hydrogel wet adhesive for internal tissue repair and anti-postoperative adhesion. Adv Funct Mater 2020;30:2005689.
[41] Yuan Z, Zhao Y, Shafiq M, Song J, Hou J, Liang Y, et al. Multi - functional fibrous dressings for burn injury treatment with pain and swelling relief and scarless wound healing. Adv Fiber Mater 2023;5:1963–85.
[42] Yu X, Shen G, Yan J, Guo W, Yuan Z, Cui J, et al. Induction of macrophage polarization by electrospun nano-yarn containing naproxen sodium to promote tendon repair. Appl Mater Today 2024;36:102070.
[43] Lei K, Chen M, Guo P, Fang J, Zhang J, Liu X, et al. Environmentally adaptive polymer hydrogels: maintaining wet-soft features in extreme conditions. Adv Funct Mater 2023;33:2303511.
[44] Xiao L, Liu H, Huang H, Wu S, Xue L, Geng Z, et al. 3D nanofiber scaffolds from 2D electrospun membranes boost cell penetration and positive host response for regenerative medicine. J Nanobiotechnol 2024;22:322.
[45] Singh RS, Walia AK, Kanwar JR. Protozoa lectins and their role in host–pathogen interactions. Biotechnol Adv 2016;34:1018–29.
[46] Teng L, Shao Z, Bai Q, Zhang X, He YS, Lu J, et al. Biomimetic glycopolypeptide hydrogels with tunable adhesion and microporous structure for fast hemostasis and highly efficient wound healing. Adv Funct Mater 2021;31:2105628.
[47] Nie W, Marrotte EJ, Xie R, Machens HG, Schilling AF, Shen Y, et al. Towards scarless repair: MMP-2 responsive drug releasing nanofibrous mat restores homeostasis via fibroblasts' activation. Composites Part B 2025;291:111972.
[48] Zhang X, Wu Y, Gong H, Xiong Y, Chen Y, Li L, et al. A multifunctional herb-derived glycopeptide hydrogel for chronic wound healing. Small 2024;20:2400516.
[49] Byun H, Han Y, Kim E, Jun I, Lee J, Jeong H, et al. Cell-homing and immunomodulatory composite hydrogels for effective wound healing with neovascularization. Bioact Mater 2024;36:185–202.
[50] Zhang L, Yuan Z, Shafiq M, Cai Y, Wang Z, Nie P, et al. An injectable integration of autologous bioactive concentrated growth factor and gelatin methacrylate hydrogel with efficient growth factor release and 3D spatial structure for accelerated wound healing. Macromol Biosci 2023;23:2200500.
[51] Huang M, Yuan Z, Fu G, Dong J, Sun Y, Wang W, et al. An injectable antibacterial wet-adhesive for meniscal cartilage regeneration via immune homeostasis mediated by SMSC-derived extracellular vesicles. Composites Part B 2025;291:111970.
[52] Shi Y, Rupa P, Jiang B, Mine Y. Hydrolysate from eggshell membrane ameliorates intestinal inflammation in mice. Int J Mol Sci 2014;15:22728–42.
[53] Ma X, Bian Q, Hu J, Gao J. Stem from nature: bioinspired adhesive formulations for wound healing. J Contr Release 2022;345:292–305.
[54] Yuan Z, Zhang L, Shafiq M, Wang X, Cai P, Hafeez A, et al. Composite superplastic aerogel scaffolds containing dopamine and bioactive glass-based fibers for skin and bone tissue regeneration. J Colloid Interface Sci 2024;673:411–25.
[55] Qi L, Fang X, Yan J, Pan C, Ge W, Wang J, et al. Magnesium-containing bioceramics stimulate exosomal miR-196a-5p secretion to promote senescent osteogenesis through targeting Hoxa7/MAPK signaling axis. Bioact Mater 2024;33:14–29.
[56] Fu Z, Li D, Cui J, Xu H, Yuan C, Wang P, et al. Promoting bone regeneration via bioactive calcium silicate nanowires reinforced poly (ε-caprolactone) electrospun fibrous membranes. Mater Des 2023;226:111671.
[57] Malliappan SP, Yetisgin AA, Sahin SB, Demir E, Cetinel S. Bone tissue engineering: anionic polysaccharides as promising scaffolds. Carbohydr Polym 2022;283:119142.
[58] Li X, Liao X, Jia Z, Liu S, Li P, Li L, et al. Biodegradable PLLA/PLGA microspheres/collagen composites for continuous soft tissue augmentation. Composites Part B 2024;283.
[59] Zhang Q, Feng X, Peng S, Li L, Xiang Y, Feng T, et al. A hydrogel derived from skin secretion of Andrias davidianus to facilitate bone regeneration. Composites Part B 2024;274:111261.